Composite Structures 382 (2026) 120107

Contents lists available at ScienceDirect

Composite Structures

journal homepage: www.elsevier.com/locate/compstruct

Rapid mechanical prediction of woven ceramic fabrics via a neural network surrogate model based on the parameterized unit cell

Zhou Jiang [a], Mingming Xu [b,*], Jian Sun [a,*], Jinsong Leng [a]

[a] Center for Composite Materials and Structures, Science Park of Harbin Institute of Technology (HIT), P.O. Box 3011, No. 2 YiKuang Street, Harbin 150080, People's Republic of China

[b] School of Science, Shenzhen Campus, Harbin Institute of Technology(HIT), Shenzhen 518000, People's Republic of China

ARTICLE INFO

Keywords:
Ceramic fiber fabric
Unit cell
Artificial neural network

ABSTRACT

Ceramic fiber fabrics are vital for high-temperature morphing skins due to their exceptional thermal stability and structural adaptability. However, their mechanical properties are strongly influenced by weave architecture, necessitating detailed and systematic characterization. Current challenges include the lack of robust predictive theoretical models and the inefficiencies of experimental methods. This study tackles these issues by developing a parametric modeling framework for 2D woven fabrics using three topological parameters, combined with an automated simulation system to evaluate tensile and shear properties through Python-driven numerical analysis. The framework demonstrates high predictive accuracy, validated by experimental data. Additionally, an artificial neural network (ANN) surrogate model employs the resulting property database to reveal correlations between weave architecture and mechanical properties. A novel integrated resistance factor is introduced to comprehensively assess mechanical performance, identifying plain weave architectures as optimal for combined tensile and shear resistance. This ANN-based surrogate model approach significantly improves efficiency in material design and performance prediction.

1. Introduction

Aircraft with variable configurations can enhance lift and drag characteristics by dynamically adjusting their aerodynamic shape, thereby optimizing flight performance across a wide range of speeds and maximizing overall aerodynamic efficiency [1]. Deformable skin is a critical technology for enabling such configuration changes [2]. However, as aircraft speeds increase within the atmosphere, traditional flexible skin materials often fail to perform reliably due to extreme aerothermal conditions [3]. To address this challenge, ceramic fiber woven fabrics have attracted significant research interest owing to their exceptional high-temperature resistance and capacity for flexible deformation under thermal loads [4–9]. For instance, Boeing's Conformal Resolvable Insulation (CRI) [7] employs borosilicate aluminum fiber fabric and quartz fiber fabric on the high- and low-temperature surfaces, respectively, retaining robust mechanical properties and flexibility even under prolonged exposure to high temperatures. Similarly, NASA's Advanced Deployable Entry Platform Technology (ADEPT) [8,10] utilizes carbon fiber fabric as a protective surface layer, enabling inflation and deployment in ultra-high-temperature environments with substantial deformation capability. This technology was successfully flight-tested in 2022 under the Low Earth Orbit Flight Test of an Inflatable Decelerator (LOFTID) project [9]. These advancements demonstrate that ceramic fiber woven fabrics exhibit outstanding high-temperature resilience and large-scale deformability in practical applications, making them indispensable for designing high-performance, heat-resistant deformable skin structures (see Fig. 1).

Ceramic fiber fabrics exhibit distinct mechanical properties depending on their weave structures, making them suitable for designing high-temperature-resistant and deformable skins tailored to diverse flight conditions. However, existing research on fabric mechanics models primarily focuses on constructing and analyzing theoretical models for specific weave types, lacking a systematic investigation into the mechanical behavior of fabrics with varying organizational structures. Experimental approaches to studying fabric mechanics often involve weaving multiple fabric types and testing their properties using specialized equipment [14,15]. This process is not only time-consuming and costly, but also impractical for comprehensive characterization due to the near-infinite variability in fabric structures driven by advancing textile technologies. Such limitations significantly hinder the design cycle of high-temperature-resistant deformable skins. To address these challenges, artificial neural network (ANN) technology has gained prominence for predicting the mechanical properties of materials and

* Corresponding authors.
E-mail addresses: mingm.xu@outlook.com, xumingming@bit.edu.cn (M. Xu), sunjian@hit.edu.cn (J. Sun).

https://doi.org/10.1016/j.compstruct.2026.120107
Received 17 August 2025; Received in revised form 6 January 2026; Accepted 27 January 2026
Available online 28 January 2026

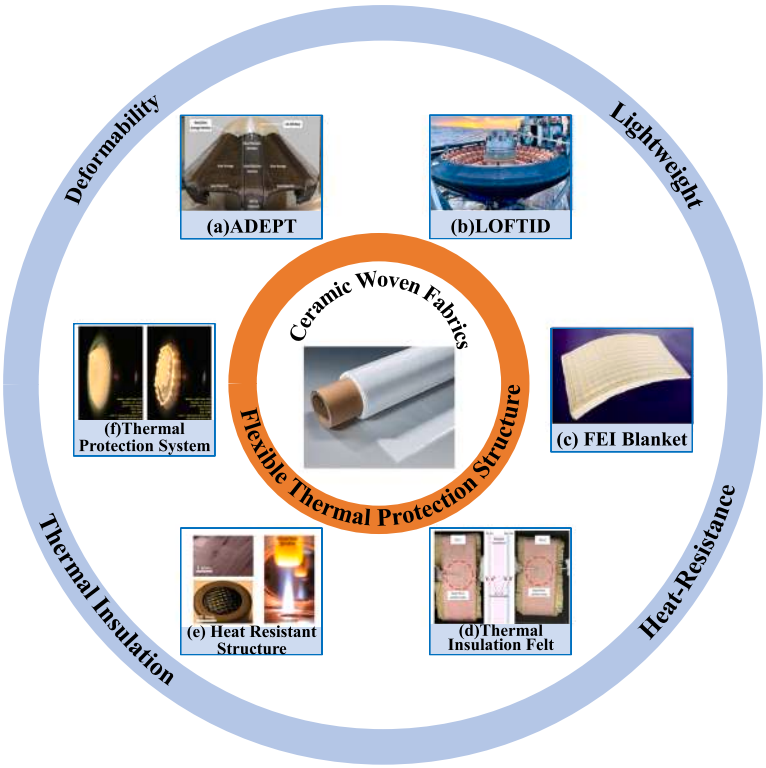

Fig. 1. Application of ceramic fiber fabrics in high-temperature deformation resistant structures: (a) schematic diagram of the inflatable decelerator structure for NASA's ADEPT project [8], (b) the inflatable decelerator test article for NASA's LOFTID project [9], (c) FEI Blanket with variable thickness [6],(d) Tensile testing of flexible insulating felts under elevated temperatures [11],(e) the plasma scouring test of the surface fabric for flexible thermal protection structures [12], (f) The flexible thermal protection system was subjected to arc-heated wind tunnel testing [13].

structures [16–18]. Its advantages include powerful non-linear fitting capabilities, data-driven modeling, and compatibility with traditional mechanical models [19–21]. Numerous researchers have applied ANNs to predict fabric mechanical properties. Minakshi Achwar [22] developed a machine learning-based ANN model that predicts warp and weft tear strength from fabric parameters, achieving a training accuracy of approximately 99.99%. Tomislav Rolich et al. [23] employed an ANN model to predict fabric ductility based on fundamental characteristics such as warp/weft density, mass per unit area, and thickness. Chamika Wanasinghe et al. [24] developed an integrated framework combining multiscale modeling and explainable machine learning to accurately predict the ABD stiffness matrix of carbon fiber woven composites based on fiber architecture, ply arrangement, and constituent properties. B. R. Gurumurthy et al. [25] designed a feedforward ANN model to estimate fabric compression performance using parameters like yarn density, ends/weft per inch, curvature, coverage, weight, thickness, bulk density, and twist. Their results demonstrated superior predictive performance compared to conventional mathematical models. These studies highlight the potential of ANN technology as a robust alternative to experimental and analytical methods for accelerating the design of advanced fabric-based skins.

This study systematically investigates the influence of weave structures on fabric mechanical properties to guide deformable skin design for high-mach-number morphing aircraft. Three key topological parameters were employed to simplify the characterization of 2D weave architectures (plain, satin, and twill). By integrating parametric modeling software with finite element analysis tools, a comprehensive analytical framework was developed for evaluating the mechanical properties of periodic diamond-shaped unit cells. This framework enabled batch generation of a mechanical property database for fabrics with diverse weave structures. Utilizing this database, a specialized artificial neural network (ANN) model was trained to rapidly predict fabric mechanical properties based on architectural topological parameters. Through the established framework combined with the ANN model, systematic analysis was conducted to elucidate how the three architectural topological parameters influence axial tensile and shear properties. For comprehensive fabric performance evaluation, a novel fabric integrated resistance factor was proposed to assess combined tensile/shear resistance characteristics. Analytical results demonstrated that plain weave structures exhibit the highest integrated resistance factor, indicating superior overall tensile and shear resistance performance compared to other weave types.

2. Parameterization method for two-dimensional woven structures

To streamline the modeling of woven fabric structures, a systematic naming convention is established based on three key architectural topological parameters: n_{up}-n_{down}-n_{step}, which follow the same unification and parameterization method of 2D and 3D weaves are used in formulating the woven fabric unit cell [26]. As shown in Fig. 2: n_{up} is the number of yarns in another system that bounce before turning (the bouncing yarns cover the yarns in the other system), n_{down} is the number of yarns in another system that bounce before turning (the bouncing yarns are covered by the yarns in the other system), n_{step} is the number of intervening yarns in the longitudinal (or transverse) direction of the closest warp (weft) interlacing point of the same nature on two adjacent yarns. In the woven fabric unit cell shown in Fig. 2, the architectural topological parameters are $n_{up} = 1$, $n_{down} = 4$, and $n_{step} = 2$, according to the parameterization method in this study, the fabric represented by the unit cell in Fig. 2 is named 1-4-2. The numerical values of the three architectural topological parameters for some common fabrics and their corresponding names are shown in Fig. 3. In the figure, the plain weave fabric is designated as 1-1-1, the twill weave fabric as 2-2-1, and the satin weave fabric as 1-5-3. This

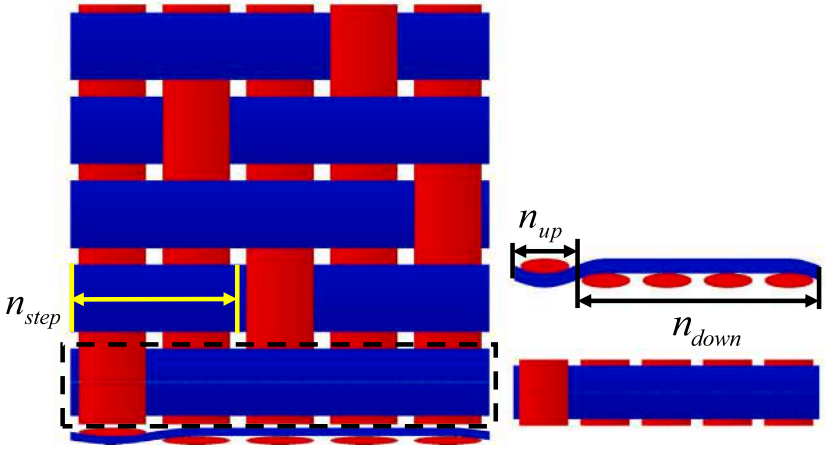

Fig. 2. Schematic diagram of fabric topological parameters definitions.

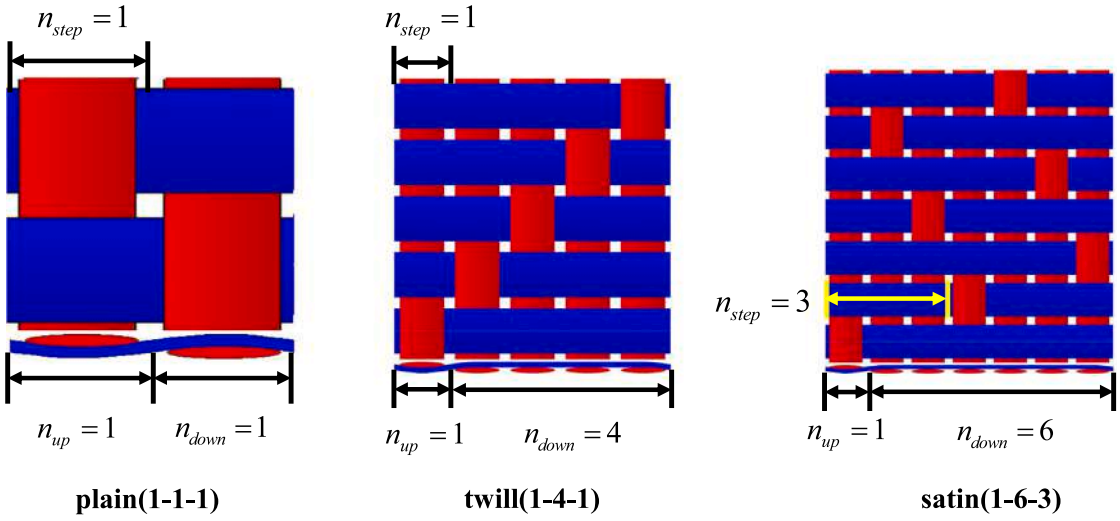

Fig. 3. Architectural topological parameters and nomenclature of common woven fabric structures (plain/twill/satin).

parameterization approach provides a rigorous and systematic framework for characterizing diverse 2D woven fabrics, enabling effective investigation of weave pattern influences on mechanical properties in subsequent analyses.

3. The finite element characterization method for mechanical properties of woven fabrics

3.1. Modeling method

The modeling module in this study is implemented through secondary development of the TexGen software [27]. By integrating Python scripts with the built-in modeling functions, automated fabric modeling is achieved, preventing yarn interpenetration while enabling the export of key information such as periodic meshes and material orientations for dry fabrics. This significantly streamlines the preprocessing workflow for finite element analysis, improving both modeling accuracy and efficiency.

3.2. Periodic boundary conditions

Fabric structures exhibit typical periodic characteristics, making them particularly suitable for finite element analysis using unit cell models. Compared to simulating the entire large-scale structure, applying periodic boundary conditions to a representative unit cell for finite element analysis can significantly simplify the computational process. This approach maintains analytical accuracy while substantially reducing computational costs. In this study, periodic boundary conditions defined by Eq. (1)–Eq. (3) were applied to the fabric unit cell structure via a Python script. Eq. (1) establishes the relationship between the displacement difference of corresponding boundary points (u, v) and (u', v') on the periodic unit cell and the macroscopic strain field(ε_x^0, ε_y^0, γ_{xy}^0) [26]:

$$\begin{Bmatrix} u' \\ v' \end{Bmatrix} - \begin{Bmatrix} u \\ v \end{Bmatrix} = \begin{bmatrix} \varepsilon_x^0 & 0 \\ \gamma_{xy}^0 & \varepsilon_y^0 \end{bmatrix} \begin{Bmatrix} \Delta x \\ \Delta y \end{Bmatrix} = \begin{Bmatrix} \varepsilon_x^0 \Delta x \\ \gamma_{xy}^0 \Delta x + \varepsilon_y^0 \Delta y \end{Bmatrix} \tag{1}$$

In the above equation, where u and v represent the original displacement components at the reference point, while u' and v' denote the displacement components at the corresponding point. The strain matrix on the right-hand side is the strain–displacement transformation matrix for a two-dimensional plane problem, where ε_x^0 and ε_y^0 are the normal strains, γ_{xy}^0 is the shear strain, Δx and Δy represent the relative coordinate differences between two points within the unit cell.

When analyzing the boundary in the x-direction (where $\Delta x = L_x$, $\Delta y = 0$), the displacement constraint reduces to:

$$\begin{Bmatrix} u' \\ v' \end{Bmatrix} - \begin{Bmatrix} u \\ v \end{Bmatrix} = \begin{bmatrix} \varepsilon_x^0 & 0 \\ \gamma_{xy}^0 & \varepsilon_y^0 \end{bmatrix} \begin{Bmatrix} \Delta x \\ \Delta y \end{Bmatrix} = \begin{Bmatrix} \varepsilon_x^0 L_x \\ \gamma_{xy}^0 L_x \end{Bmatrix} \tag{2}$$

Table 1
Quartz yarn information.

Manufacturer	Type	Monofilament Diameter (μm)	Linear Density (tex)
Feilihua Quartz Glass Co., Ltd	Type B	7.5	190

When analyzing the boundary in the y-direction (where $\Delta x = 0$, $\Delta y = L_y$), the displacement constraint reduces to:

$$\begin{Bmatrix} u' \\ v' \end{Bmatrix} - \begin{Bmatrix} u \\ v \end{Bmatrix} = \begin{bmatrix} \varepsilon_x^0 & 0 \\ \gamma_{xy}^0 & \varepsilon_y^0 \end{bmatrix} \begin{bmatrix} 0 \\ L_y \end{bmatrix} = \begin{Bmatrix} 0 \\ \varepsilon_y^0 L_y \end{Bmatrix} \tag{3}$$

The equations above establish a quantitative relationship between the macroscopic strain and the unit cell characteristic dimensions (L_x, L_y). When the unit cell deforms under an applied macroscopic strain field, the displacement difference between corresponding boundary points must strictly maintain a proportional relationship with the macroscopic strain. This constraint ensures displacement continuity between the deformed unit cell boundaries and the adjacent cells, thereby preserving the overall kinematic compatibility of the structure. To prevent over-constraining the system, a reference node strategy combined with multi-point constraint (MPC) equations is employed to implement the periodic boundary conditions. The specific procedure is as follows: First, a reference node is placed at one vertex of the unit cell, and its in-plane translational degrees of freedom (u, v) are fully constrained to eliminate rigid-body translation of the entire model. Subsequently, based on the relationship between macroscopic strain and relative displacement described by Eq. (1)–Eq. (3), MPC equations are applied to enforce the relative displacement constraints between all pairs of periodic boundary nodes. This approach restricts only the relative motion between boundary nodes, while allowing the unit cell to undergo rigid-body rotation under the macroscopic strain field, thereby avoiding the introduction of non-physical constraint forces. By establishing the relationship between the macroscopic strain field and the unit cell dimensions and adopting the above constraint strategy, the present model accurately captures the macroscopic mechanical behavior of the overall structure. This ensures both mathematical completeness of the boundary conditions and physical consistency of the model, thereby guaranteeing the representativeness and reliability of the unit cell simulation results.

3.3. Calibration of yarn parameters (E_1)

Quartz fiber fabric exhibits outstanding thermal stability, along with a mature manufacturing process, high cost-effectiveness, and broad applicability. As a result, it is widely used in aerospace and high-temperature insulation applications. Being a representative ceramic fiber fabric, it is selected in this study to investigate the influence of unit cell architectural topological parameters on the mechanical properties of woven fabrics.

Quartz fiber fabric is a two-dimensional flexible structure composed of interwoven quartz yarns, which serve as the fundamental building blocks of the fabric. Prior to finite element modeling of the fabric structure, a thorough understanding of the mechanical behavior of quartz yarns is essential. The axial tensile properties of the yarns (data shown in Table 1) were experimentally characterized in accordance with DIN EN ISO 2062:2010 standard for yarn property testing, using an electronic universal testing machine equipped with arc-shaped fiber grips. Three yarn specimens were extracted from the same spool, each prepared with an effective gauge length of 500 mm. Special attention was paid to ensuring proper alignment of the specimens with the applied force direction and maintaining tautness during grip tightening. Tensile tests were conducted at a constant speed of 200 mm/min. The force and displacement data were recorded by the machine's built-in sensors and then converted into stress and strain using Eqs. (4) and (5), respectively.

$$\varepsilon = \frac{\Delta l}{l_0} \tag{4}$$

$$\sigma = \frac{F}{Tt/\rho} \tag{5}$$

Where ε represents the axial tensile strain of the yarn, Δl represents the elongation of the yarn, and l_0 represents the initial length of the sample; σ represents the axial tensile stress of the yarn, F represents the tensile force read by the electronic universal testing machine; Tt represents the linear density of the yarn, which is 190 tex (provided by the manufacturer); ρ represents the density of the yarn fibers, which is 2.2 g/cm^3 (provided by the manufacturer).

The resulting stress–strain curves of the yarn under axial tension are presented in Fig. 4. The tensile modulus of each yarn sample was obtained by linearly fitting the initial elastic region of the corresponding stress–strain curve. The calculated moduli of the three samples were 76.09 GPa, 77.45 GPa, and 77.98 GPa, respectively, yielding an average tensile modulus of 77.17 GPa for the yarn.

To further investigate the applicability of quartz products under high-temperature conditions such as deformation skin, this study systematically performed high-temperature heat-treatment experiments on quartz yarn and examined its modulus evolution. A quartz-lamp radiation heating system was employed to rapidly heat the yarn specimens—reaching the target temperature within 10 s and maintaining it for 5 min. Target temperatures were set at 200 °C, 400 °C, 600 °C, and 800 °C to simulate short-term thermal exposure in high-temperature environments. After heat treatment, specimens were prepared in compliance with the DIN EN ISO 2062:2010 standard. To ensure uniform heating and precise temperature control, all test samples were taken from yarn segments located near the central region of the quartz-lamp radiation zone. Additionally, to prevent the influence of geometric defects, such as bends or kinks, on tensile test results, each specimen was extracted from a straight portion of the yarn, avoiding any areas of localized deformation caused by contact or support. The tensile modulus of the quartz yarn was measured, and the results are presented in Fig. 5. As shown in the figure, within the temperature range from 25 °C to 600 °C, the modulus of the quartz yarn remains remarkably stable, maintaining a value of approximately 77 GPa without significant degradation. This stability highlights the excellent high-temperature mechanical performance of the material. Such behavior can be attributed to the structural nature of quartz fibers, which consist predominantly of amorphous SiO_2. At moderately elevated temperatures, this amorphous network remains largely intact, undergoing neither distinct glass transition nor notable thermal decomposition, thus preserving the fiber's stiffness. When the temperature is increased to 800 °C, a discernible reduction in modulus is observed, which is likely associated with the initiation and propagation of surface microcracks. Nevertheless, the retained modulus remains relatively high, further underscoring the high-temperature capability of quartz-based materials and their suitability for applications in thermally demanding environments.

3.4. Calibration of yarn parameters (other essential mechanical properties)

Quartz fiber yarn exhibits distinct anisotropic characteristics. While its axial Young's modulus (E_1) can be directly measured using conventional tensile testing, other essential parameters required for finite element analysis — including transverse Young's moduli (E_2, E_3), Poisson's ratios(ν_{12}, ν_{13}, ν_{23}), and shear moduli (G_{12}, G_{13}, G_{23}) - are challenging to determine accurately through experimental methods alone. This difficulty arises from several factors: the submillimeter diameter of yarn makes it impractical to prepare standardized specimens for transverse tensile or shear testing; applying uniform transverse

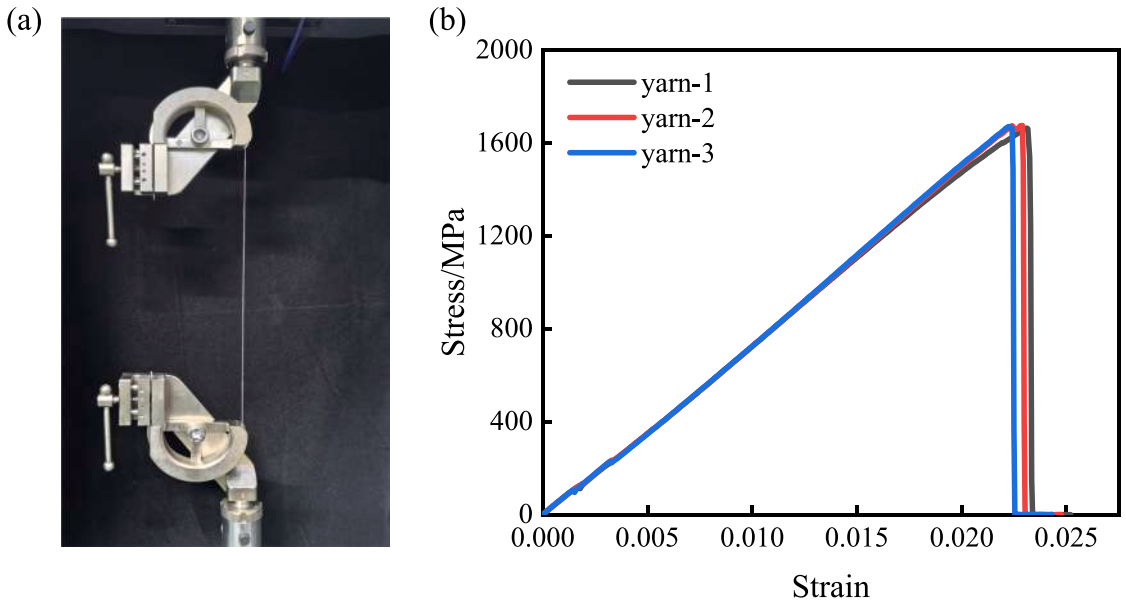

Fig. 4. (a) Yarn mechanical performance testing experiment. (b) Quartz fiber yarn axial tensile strain-stress diagram.

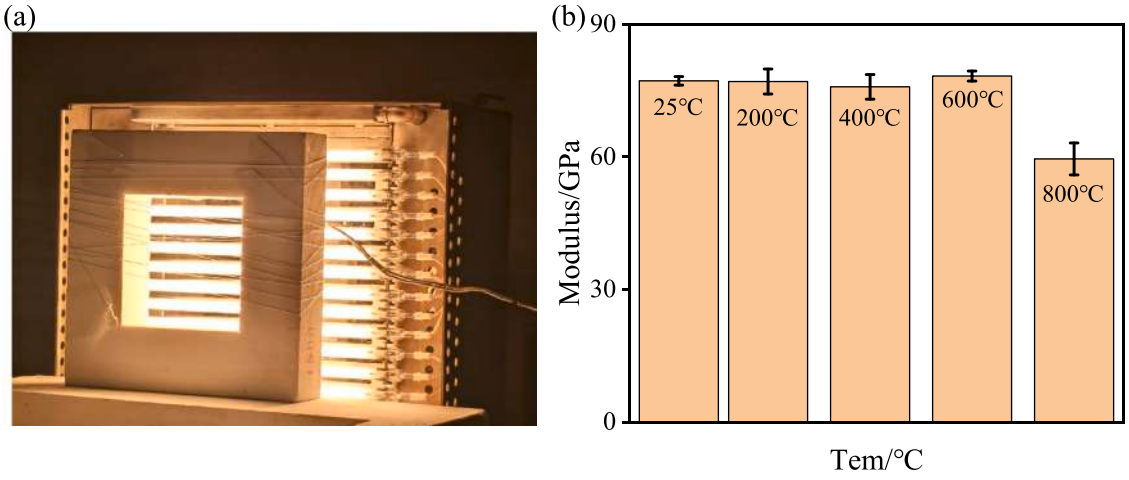

Fig. 5. (a) High temperature heat treatment of quartz yarn. (b) Evolution of quartz yarn modulus with heat treatment temperature.

clamping or pure shear loading at this scale is technically challenging; and the internal structure of the yarn, comprising thousands of individual ceramic fibers with complex interfacial friction, slippage, and entanglement, leads to highly coupled mechanical responses under bias loading that are difficult to isolate and quantify experimentally. Furthermore, experimentally measured inter-yarn friction coefficients often show considerable scatter and poor reliability. Currently, international standards such as ASTM and ISO focus primarily on axial tensile properties, twist, and breaking strength of yarns, with no widely accepted test protocols for transverse or shear behavior. To address these limitations, this study adopts an experimental calibration approach to determine the material parameters necessary for numerical simulation. The methodology consists of three key steps: first, the mechanical properties of the yarn are established through tensile and shear tests on quartz fiber fabric. Second, considering that ceramic fiber yarns consist of multiple bundled fibers—resulting in transverse stiffness and shear moduli substantially lower than the axial modulus [28]—appropriate initial estimates for these parameters are introduced. Finally, finite element simulations are performed iteratively while adjusting the transverse moduli, Poisson's ratios, shear moduli, and friction coefficients until excellent agreement is achieved between the simulated and experimental results. The final validated set of parameters is then employed in subsequent analyses.

(1) Axial and bias tensile tests on quartz fabrics

For experimental validation, this study employed the quartz plain woven (the information is shown in Table 2) made from the aforementioned test quartz yarns as the test material. The test specimens (150 mm x 25 mm) were prepared from non-edge areas of a 1-meter-long fabric sample in accordance with ASTM D5035-11(2015) standard for textile testing. Aluminum tabs (25 mm x 25 mm), cleaned with alcohol and polished, were bonded to both ends of each specimen to ensure proper load transfer. The instrumented specimens were then mounted in the testing machine and subjected to uniaxial tension at a constant rate of 50 mm/min (Fig. 6(a)). Force–displacement data were recorded using the testing machine's integrated sensors and subsequently processed using Eqs. (4) and (6) to obtain the tensile stress–strain response of the plain-woven quartz fabric (Fig. 6(c)).

$$\sigma = \frac{F}{bt} \tag{6}$$

Where F represents the tensile force read by the electronic universal testing machine; b is the width of the specimen, which is 25 mm; t is the thickness of the fabric, which is 0.1 mm.

Table 2
Quartz woven information.

Manufacturer	Type	Thickness (mm)	Warp/Weft Density (ends/cm)
Feilihua Quartz Glass Co., Ltd	QWB100A	0.1	20

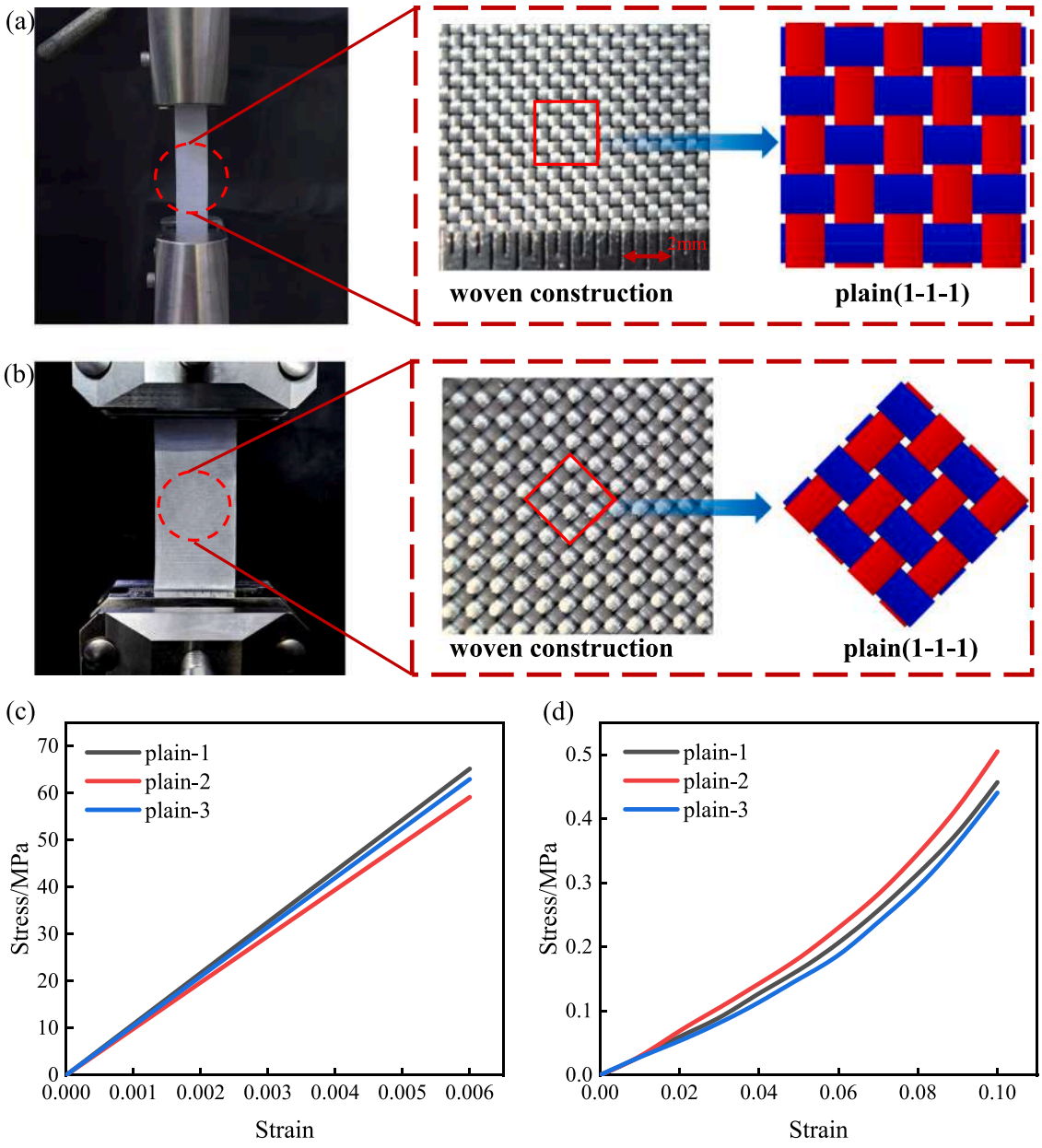

Fig. 6. Mechanical properties test diagram and experimental data of plain weave quartz fabric: (a) axial tensile test, (b) bias tensile test, (c) axial tensile stress–strain curve, (d) bias tensile stress–strain curve.

Following the same experimental approach, the bias tensile method was employed to evaluate the shear properties of plain-woven quartz fabric, adopting the measurement protocol established in literature [29]. Prior to specimen preparation, the outermost layer of the fabric roll was removed to eliminate potential surface damage. From the remaining material, a 1-meter sample was obtained, from which three test specimens (200 mm x 50 mm) were carefully extracted. To ensure proper load transfer during testing, 50 mm x 50 mm aluminum reinforcement plates were prepared through thorough cleaning with alcohol and subsequent polishing. These plates were then bonded to both ends of each specimen, resulting in an effective test area of 100 mm x 50 mm (length-to-width ratio = 2). This dimensional ratio was specifically chosen to enhance experimental reproducibility. The prepared specimens were mounted in the testing machine as illustrated in Fig. 6(b). Tensile tests were conducted at a constant displacement rate of 10 mm/min, with force and displacement data being recorded through

the testing machine's integrated sensors. The bias tensile stress–strain response of the plain-woven quartz fabric was subsequently derived using Eqs. (4) and (7), with representative results shown in Fig. 6(d).

$$\sigma = \frac{F}{\sqrt{2}bt} \tag{7}$$

Notably, the bias tensile test described above actually reflects the shear behavior of the fabric. For 2D woven fabrics, there are two widely recognized methods for characterizing shear behavior in the industry: one is the picture-frame shear test, and the other is the bias tensile test. In the bias tensile test, the warp and weft yarns of the fabric are oriented at 45° to the loading direction. During stretching, the yarns rotate, resulting in in-plane shear deformation of the fabric structure. For specific testing procedures, relevant literature [29] can be referred to. This also explains why the stress magnitude in Fig. 6(d) is much lower than that in Fig. 6(c). Under bias tension, the in-plane shear response of the fabric is primarily governed not by fiber axial stretching, but by shear-induced rotation and slippage between yarns. The stress in this process mainly originates from inter-yarn friction, which is considerably lower than the stress level associated with the tensile strength of fibers in the warp and weft directions. The increase in stiffness (tangent modulus) with loading observed in Fig. 6(d) can be attributed to the following mechanism: at low load levels, the load is primarily borne by inter-yarn friction and bending stiffness, resulting in relatively low overall stiffness. As shear deformation increases, significant rotation occurs within the yarn system of the fabric, gradually aligning the yarns with the loading direction. Since the axial tensile modulus of the yarns themselves is much higher than their shear and bending moduli, this structural rearrangement leads to macroscopic apparent strain hardening, i.e., an increase in stiffness with rising load.

(2) Material parameters analysis of quartz yarn

In the finite element analysis of the plain-woven fabric unit cell, the yarn material is modeled as an orthotropic elastic continuum, with its material parameters defined according to the following relations: $E_1 \gg E_2 = E_3 \approx G_{12} = G_{13} = G_{23}$ and $\nu_{12} = \nu_{13} = \nu_{23} \approx 0$. This parameterization is grounded in the microstructural characteristics and macroscopic mechanical behavior of the yarn. As a bundle composed of thousands of parallel ceramic fibers, the yarn exhibits high stiffness along the fiber direction (longitudinal), governed primarily by the intrinsic modulus of the fibers, which justifies the high value of E_1. In the transverse directions, however, mechanical response is dominated by weak inter-fiber friction and contact, resulting in substantially lower stiffness. Given the approximately axisymmetric cross-section of the yarn, the transverse moduli are set equal, i.e., $E_2 = E_3$, with values orders of magnitude lower than E_1. Similarly, the shear moduli in all directions are assigned values comparable to the transverse moduli, reflecting the prevalent role of fiber sliding rather than material shear. The Poisson's ratios are approximately equal to zero, consistent with the microscale slip mechanism within the yarn bundle: under longitudinal tension, fibers can rearrange with minimal lateral constraint, leading to negligible transverse contraction. This simplified yet physically representative parameter set effectively captures the essential yarn behavior—"stiff in tension along the fibers, compliant in transverse and shear directions"—and aligns with widely adopted modeling practices in mechanics of dry fabrics . The approach is further supported by existing literature [28].

(3) Iterative analysis based on finite element method

Based on the established parameters, the single-unit cell model of the plain-woven fabric was first developed using TexGen 3.12.2 and subsequently imported into ABAQUS 2022. In ABAQUS, a finite element model was constructed with the application of periodic boundary conditions to simulate the macroscopic mechanical response of the material. The constitutive behavior of the yarns was represented by an orthotropic linear elastic material model. The mesh primarily consisted of C3D8 hexahedral elements, with C3D6 triangular prism elements used locally at edges to conform to the geometry, balancing accuracy and computational cost.

The interaction between yarns was modeled using a surface-to-surface contact algorithm: normal behavior was defined as "hard contact" to prevent penetration, and tangential behavior was governed by a penalty-based friction model to account for frictional effects during relative sliding. The numerical simulations included two typical loading scenarios:

- axial strain application along the yarn directions to replicate the fabric's tensile performance (Fig. 7(a))
- bias strain application at 45° to the warp/weft directions to simulate shear behavior (Fig. 7(b))

Based on an iterative calibration approach, the system adjusted the transverse modulus, Poisson's ratio, shear modulus, and inter-yarn friction coefficient, modifying parameters such as the shear modulus G, friction coefficient μ, and transverse modulus $E_2 = E_3$. The system evaluated their influence on the tensile and shear behavior of the fabric. As shown in Figs. 8(a) and 8(b), when G was set within the range of 0.2–0.3 GPa, the simulated stress–strain curves exhibited the best agreement with experimental results, indicating that shear moduli in this range accurately reflect the actual inter-yarn shear stiffness. In contrast, values of G that were too high or too low caused the simulated curves to deviate noticeably from the experimental trend. Regarding the influence of the friction coefficient (Fig. 8(c)), a value of $\mu \approx 0.5$ effectively reproduced the transition from linear to nonlinear deformation observed in experiments, whereas lower friction resulted in excessive yarn slippage and an overall softer response. The effect of the transverse modulus is shown in Fig. 8(d). When $E_2 = E_3 = 0.5$ GPa, the simulated initial stiffness and overall deformation trend aligned most closely with experiments, suggesting that moderate transverse constraints appropriately characterize the internal interactions within the fabric under tension. Additionally, variations in Poisson's ratio within the range of 10^{-5} to 10^{-9} produced no visible differences in the curves, indicating its negligible influence on the in-plane mechanical behavior of the fabric. In summary, through parameter adjustment and experimental comparison, a set of yarn material parameters capable of accurately characterizing the mechanical behavior of plain-weave quartz fabric was determined, as listed in Table 3.

Through an iterative calibration process, the transverse Young's modulus, Poisson's ratio, shear modulus, and inter-yarn friction coefficient were systematically adjusted until excellent agreement between simulated and experimental tensile/shear responses was achieved (Fig. 8). The final validated material parameters, as summarized in Table 3, were subsequently employed for all further finite element analyses. It should be noted that experimental results show the axial tensile modulus E_1 of quartz yarn remains stable at approximately 77 GPa from 25 °C to 600 °C, indicating excellent high-temperature stability. However, the material parameters in Table 3 were calibrated from mechanical tests conducted at room temperature and are therefore only applicable for analyzing the fabric's mechanical behavior under room temperature conditions.

3.5. Determination of irrelevance in finite element analysis

The unit cells of fabrics typically consist of only a few yarns, exhibiting size differences spanning multiple orders of magnitude compared to actual engineering-scale fabrics (Fig. 9). Furthermore, substantial size variations exist among unit cells of different fabric structures. To validate the size independence of the computational method, finite element simulations must be performed using models of the same fabric structure across varying scales. This ensures that the numerical results are not influenced by size effects.

As illustrated in Fig. 10, three plain weave fabric unit cells of varying sizes were analyzed, labeled as "2 x 2", "4 x 4", and "6 x 6" to denote the number of yarns along the warp and weft directions. The area of each unit cell increases proportionally with the number of yarns . Specifically, the "6 x 6" unit cell (with the highest yarn count) exhibits an area nine times larger than that of the "2 x 2" unit cell (with the

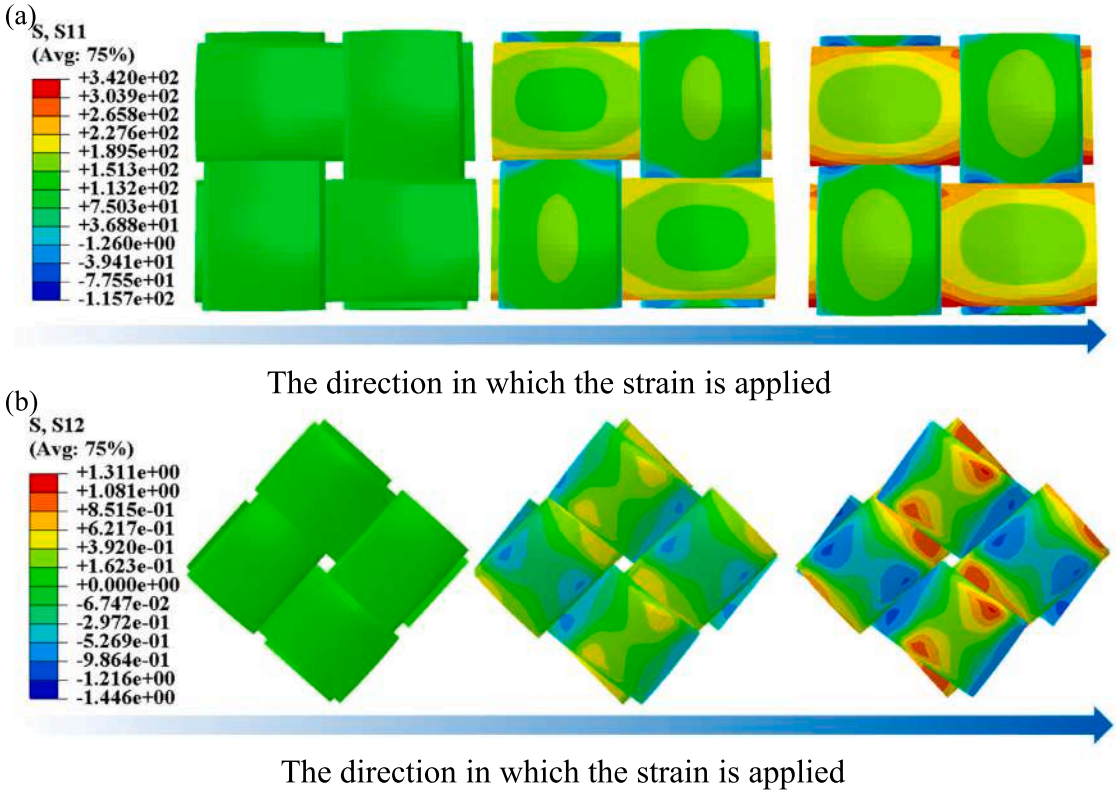

Fig. 7. (a) Finite element analysis of the axial tensile properties of plain weave fabric. (b) Finite element analysis of the bias tensile performance of plain weave fabric.

Table 3
Material Parameters of Quartz Yarn.

E_1	E_2	E_3	ν_{12}	ν_{13}	ν_{23}	G_{12}	G_{13}	G_{23}	$Fric$
77.17 GPa	0.5 GPa	0.5 GPa	$10E-7$	$10E-7$	$10E-7$	0.25 GPa	0.25 GPa	0.25 GPa	0.5

lowest yarn count), representing a full order of magnitude difference. By comparing the finite element analysis results across these scales, the presence or absence of size effects in the computational methodology can be rigorously assessed.

The bias tensile response of fabric unit cells was numerically investigated using a Python implementation. Strain was applied at a 45° orientation to both warp and weft directions to simulate bias loading conditions. Fig. 11(a) presents the resulting force–deformation curves for different unit cell sizes. The results demonstrate that under identical strain conditions, the reaction force increases proportionally with fabric size. To eliminate size effects, the reaction forces were normalized using Eq. (8), with the smallest plain weave unit cell ("2 x 2") serving as the baseline. The normalized stress–strain curves shown in Fig. 11(b) reveal remarkable consistency across different unit cell sizes, as evidenced by the nearly identical curves. Moreover, stress distribution analysis indicates that:

- the deformation patterns remain consistent across different unit cell sizes at equivalent strain levels
- the stress distribution profiles are identical regardless of unit cell size
- peak stresses consistently occur at yarn intersection points

These findings confirm that the mechanical response of the fabric unit cell is independent of its size, validating the computational approach for multiscale analysis.

$$\overline{\sigma} = \sqrt{2}\frac{F}{ltn_{\text{yarn}}} \tag{8}$$

Where F represents the reaction force under bias tension of the unit cell, l denotes the unit cell size, t is the unit cell thickness, and n_{yarn} indicates the number of yarns contained in the unit cell, which is a dimensionless quantity

Prior to constructing a neural network database for the mechanical properties of fabric unit cells through batch computations, mesh independence verification is essential to ensure the accuracy and reliability of subsequent simulation results. The modeling software TexGen facilitates the generation of finite element meshes with varying densities by adjusting the Resolution function parameter during the export of unit cell models. For this study, plain weave fabric unit cells were exported with Resolution values of 40 (the default software setting), 60, and 80, corresponding to mesh counts of 7200, 16,560, and 29,440, respectively. Bias tensile tests were then simulated to evaluate mesh independence. As illustrated in Fig. 12, the stress–strain curves obtained from these simulations exhibit a high degree of overlap across all mesh densities, indicating that the results remain consistent as the mesh is refined. This conclusion is further supported by the uniform stress distributions observed in the unit cell stress maps for all three cases.

3.6. Rationality verification of finite element model

Axial and bias tensile experiments were performed on twill quartz fabric structures of identical specifications (twill 1-3-1) to validate the rationality of the finite element analysis, as illustrated in Fig. 13. All tests were repeated three times, and the results demonstrated high repeatability. To accurately compare the stiffness response between simulation and experiment in the axial tensile curves, a tangent translation was applied to the simulated curve. This adjustment was necessary

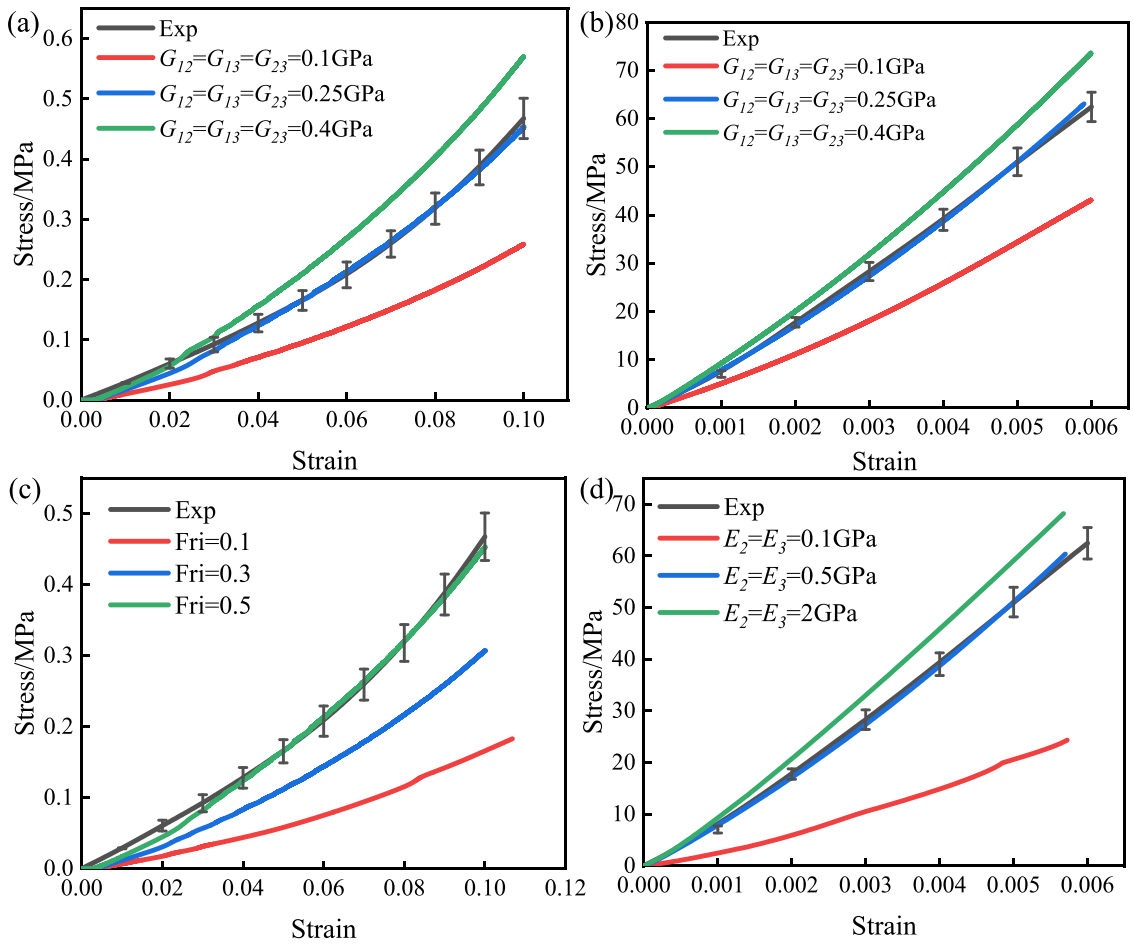

Fig. 8. (a) Comparison of bias tensile curves between finite element analysis and experiments of plain weave quartz fiber fabric under different shear modulus. (b) Comparison of axial tensile curves between finite element analysis and experiments of plain weave quartz fiber fabrics with different shear modulus. (c) Comparison of bias tensile curves between finite element analysis and experiments of plain weave quartz fiber fabric under different coefficients of friction. (d) Comparison of axial tensile curves between finite element analysis and experiments of plain weave quartz fiber fabrics with different transverse Young's modulus.

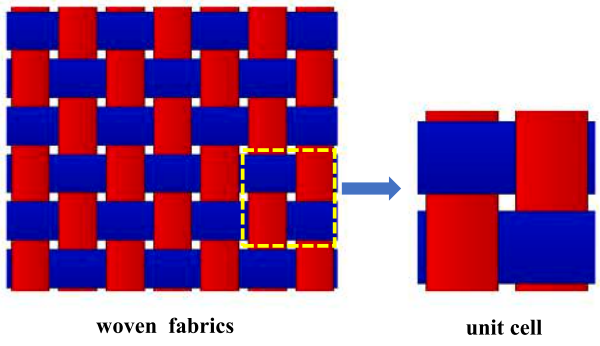

Fig. 9. Schematic diagram of a plain weave fabric unit cell.

because the experimental procedure included a preloading phase at the initial stage, which effectively bypassed the low-stiffness region caused by yarn crimping and interlacing in the fabric. As a result, the experimental data were recorded starting from an approximately linear elastic stage. By aligning the initial tangent stiffness segment of the simulation results with the experimental curve, a more reasonable comparison could be made regarding their consistency during the main load-bearing phase, thereby avoiding misinterpretation of the overall mechanical behavior due to differences in the initial nonlinear segment. The processed comparison results show that the simulated and experimental curves agree well in both the elastic stage and the subsequent deformation range, indicating that the established finite element model can effectively predict the mechanical response of the fabric under axial tension. Furthermore, the bias tensile experimental curves exhibit a consistent trend with the simulation results, further verifying the applicability of the finite element model under complex stress states.

4. Artificial neural network for fabric mechanical properties

The finite element analysis (FEM) methods described above enable the efficient determination of mechanical properties for fabric unit cells with diverse structures. Compared to traditional experimental approaches, this computational strategy substantially reduces both cost and processing time. Nevertheless, simulations of large-sized unit cells often require tens of hours to complete, posing a bottleneck for rapid design iterations. To further minimize the time investment in obtaining fabric mechanical properties and accelerate the design cycle of fabric-based skin structures, this study proposes a neural network-based predictive model. This framework facilitates the rapid estimation of mechanical behavior for fabrics with varying architectures, offering a computationally efficient alternative to conventional FEM.

4.1. Data set

A high-quality dataset is essential for training an accurate neural network. As shown in Fig. 14, the dataset generation process in

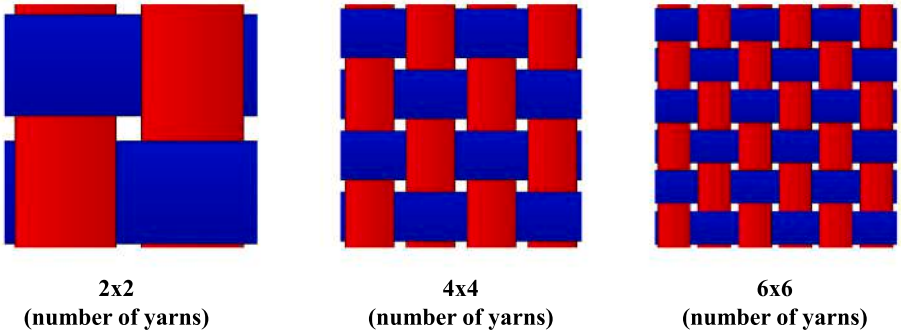

Fig. 10. Unit cell structures of plain weave fabric with different sizes.

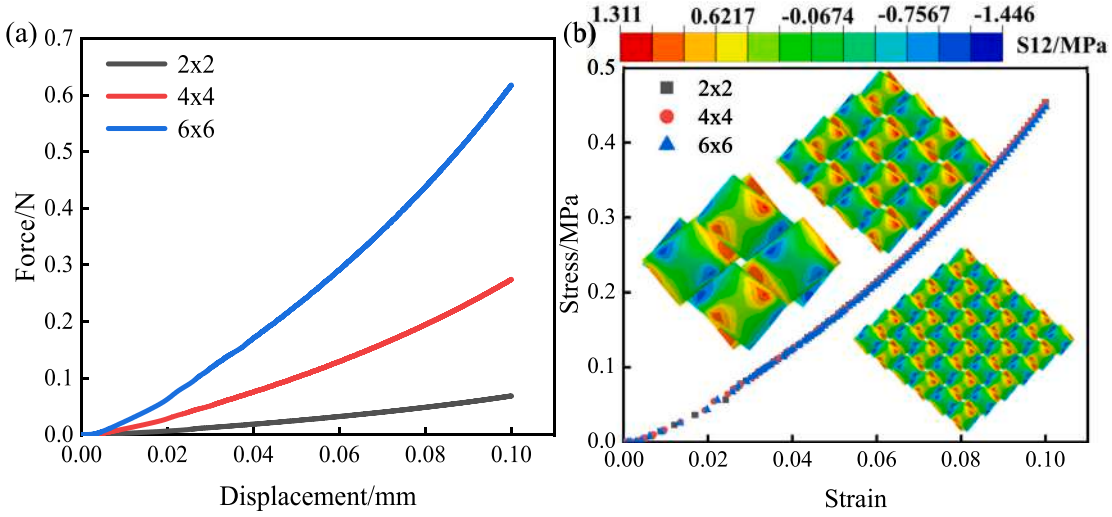

Fig. 11. (a) Simulated bias tensile force–displacement curves of plain weave fabric unit cells of different sizes. (b) Bias tensile stress–strain curves of plain weave fabric unit cells of different sizes.

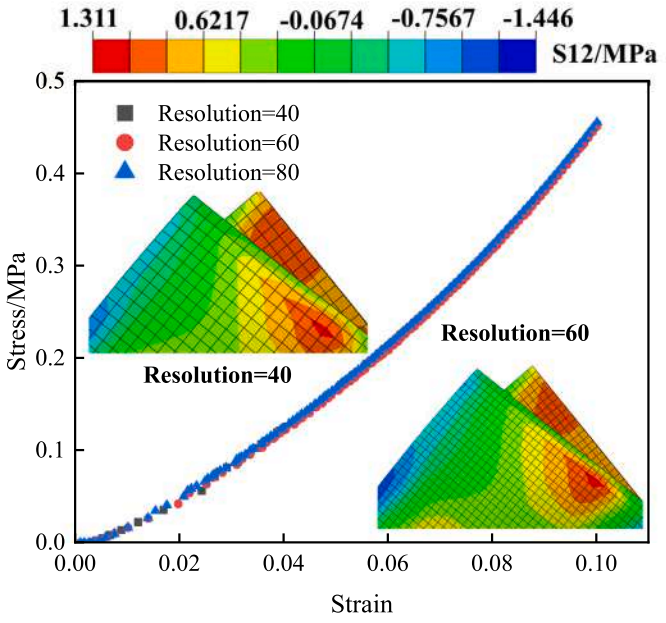

Fig. 12. Bias tensile stress–strain curves of plain weave fabric unit cell structure under different mesh quantities.

this study involves four main steps. First, the weave parameters are carefully selected to balance computational efficiency and structural diversity: n_{up} ranges from 1 to 7, n_{down} ranges from n_{up} to 7, and n_{step} is set to 1 for plain and twill weaves. For satin weaves (n_{up}+$n_{down} \geq 5 \neq 6$), n_{step} is chosen such that $1 < n_{step} < n_{up} + n_{down} - 1$ and n_{step} is coprime with $n_{up} + n_{down}$. Next, the fabric unit cell models are generated using TexGen software based on the determined parameters (n_{up}, n_{down}, n_{step}). Material properties, periodic boundary conditions, and constraints are then applied to the models through Python scripting. The center point of each unit cell is fixed, and strain is applied at 0°/90° (axial) or 45° (bias) to simulate tensile behavior. Finally, after completing the finite element simulations, Python scripts extract force–displacement data from the ODB files and compile them with the corresponding weave parameters into an Excel file. This systematic approach ensures the creation of a comprehensive dataset for neural network training while maintaining computational efficiency.

The axial and bias tensile behaviors for 41 distinct fabric unit cell configurations were simulated following the aforementioned dataset generation methodology. This process yielded two comprehensive datasets: one containing 41 axial tensile test results and another with 41 corresponding bias tensile measurements, twenty stress–strain data points were extracted from each experimental result as input data for subsequent analysis. To optimize model performance, all input data were normalized using the StandardScaler method from scikit-learn (Eq. (9)). This preprocessing step transforms the data to have zero mean and unit variance ($\mu = 0$, $\sigma = 1$), effectively converting the features to follow a standard normal distribution. The complete dataset was

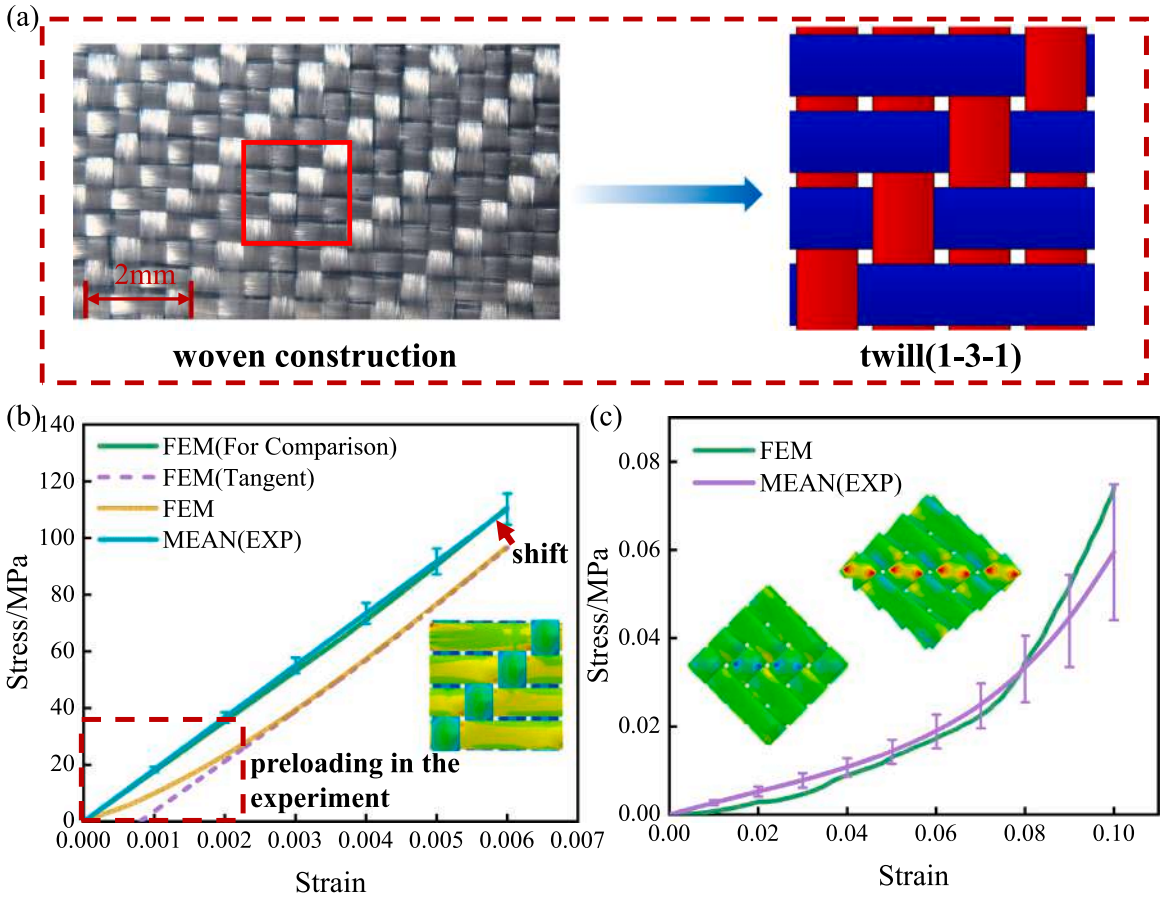

Fig. 13. (a) Twill woven construction and unit cell model. (b) Comparison between axial tensile testing and finite element analysis of twill fabric. (c) Comparison between bias tensile testing and finite element analysis of twill fabric.

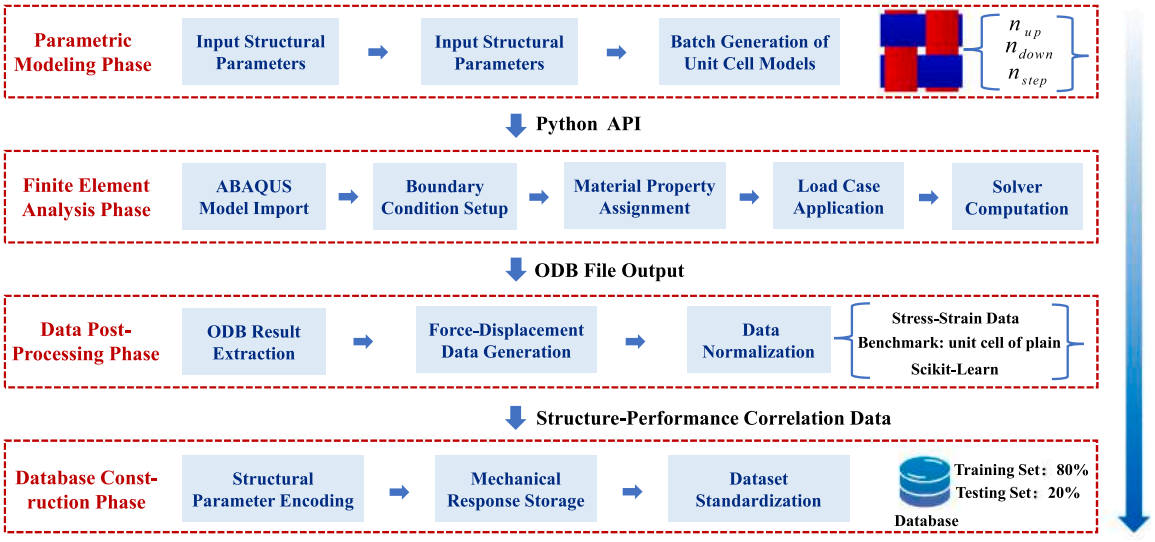

Fig. 14. Schematic diagram of the neural network training dataset generation process.

then partitioned into training and testing subsets using an 80:20 ratio, ensuring sufficient data for both model development and validation.

$$x_{\text{scaled}} = \frac{x - x_{\text{mean}}}{x_{\text{standard\_deviation}}} \tag{9}$$

x represents the original data point, x_{mean} represents the mean of the dataset, $x_{standard\_deviation}$ represents the standard deviation of the dataset, and x_{scaled} represents the normalized data point.

4.2. Construction of artificial neural networks

Artificial neural networks (ANNs), particularly deep neural networks (DNNs), represent a powerful class of machine learning algorithms composed of interconnected processing units (neurons) with well-defined input–output transformations. These neurons are organized in multi-layered architectures and connected through nonlinear activation functions, enabling the learning of highly intricate patterns. Through iterative adjustment of synaptic weights, deep ANNs can approximate complex, nonlinear relationships in labeled training data, achieving superior generalization performance on unseen data.

To predict the mechanical response of fabric structures under displacement loading, a 5-layer deep fully connected neural network (FCNN) was designed (Fig. 15). The network accepts 4 input features, comprising 3 unit cell architectural topological parameters and strain load data. These features are passed through the first fully connected layer, which transforms the input into a 32-dimensional representation. The ELU activation function is then applied to introduce nonlinearity, defined as:

$$\text{ELU}(x) = \begin{cases} x & \text{if } x \geq 0 \\ e^x - 1 & \text{if } x < 0 \end{cases} \tag{10}$$

The hidden layers utilize the Exponential Linear Unit (ELU) activation function to introduce nonlinearity. ELU mitigates the "dying neuron" problem common to other activations (e.g., ReLU) by maintaining non-zero gradients for negative inputs, while centering activations near zero to accelerate training convergence. This ensures consistent and effective nonlinear feature transformation across the three hidden layers (32–64–32 neurons). The output layer consists of a single linear unit without any activation function. It receives the 32-dimensional feature vector from the last hidden layer and performs a final linear transformation to produce a scalar stress prediction. Omitting the nonlinear activation is critical for this regression task, as it preserves the full dynamic range of the output, allowing the model to predict both axial tensile and bias tensile stress values without constraint. This design ensures that the network can accurately represent the complete mechanical response of the fabric structure. Together, the ELU-activated hidden layers and the linear output layer form an expanding-contracting hierarchical architecture (4→32→64→32→1), which enables the network to learn multi-scale representations of fabric deformation behavior while delivering physically interpretable stress predictions.

4.3. Training results and comprehensive analysis

(1) Model training dynamics and performance

The integrated analysis of Figs. 16 and 17 provides fundamental insights into the neural network's learning behavior and predictive capacity for fabric tensile characterization. Fig. 16(a) exhibits an exponential reduction in mean squared error loss during training for both deformation modes, achieving stable values of 5.11×10^{-7} (axial) and 1.25×10^{-6} (bias), while Fig. 16(b) documents corresponding R^2 values rapidly approaching unity (0.998 axial, 0.982 bias), confirming excellent capture of intrinsic mechanical relationships. These training characteristics find strong confirmation in Fig. 17, where the near-perfect coincidence of predicted and FEM reference values along the identity line for both axial (Fig. 17(a)) and 45° bias (Fig. 17(b)) loading demonstrates outstanding generalization capacity. Of particular significance is the model's accurate representation of nonlinear bias response in the low-stress regime (0–0.05 MPa), as manifested by the highly concentrated data distribution in Fig. 17(b). The remarkable agreement between training evolution (Fig. 16) and independent test predictions (Fig. 17) establishes the model's engineering-ready accuracy across diverse loading conditions — from MPa-range axial tension to sub-MPa bias deformation — without exhibiting overfitting tendencies. This verification dual approach, combining training metrics with independent test set validation, furnishes conclusive evidence for the model's reliability in simulating sophisticated fabric mechanical behavior.

(2) K-Fold cross-validation and uncertainty interval analysis

To validate the generalizability of the neural network models, an identical five-fold cross-validation framework was employed to systematically evaluate the prediction models for both axial and bias tensile loading modes. In terms of experimental setup, to ensure comparability and reproducibility, all models adopted a fully connected architecture of 4-32-64-32-1, ELU activation functions, and mean squared error loss. Data partitioning was performed with shuffling based on a fixed random seed (42). During preprocessing, each fold was independently normalized using a MinMaxScaler fitted on the entire training set to prevent data leakage. In the training process, the Adam optimizer, early stopping, and dynamic learning rate scheduling were incorporated to ensure convergence stability and mitigate overfitting. Regarding the results (Table 4), the axial tensile model demonstrated outstanding fitting performance across all five folds. The R^2 values on the validation sets all exceeded 0.9997, while those on the corresponding test sets were no lower than 0.9991. Both validation and test losses remained consistently within the order of 10^{-5} to 10^{-6}, indicating that the model possesses excellent predictive accuracy and generalization robustness for typical tensile behavior. In contrast, the bias tensile model also performed strongly on the validation sets, with R^2 above 0.9998 across all five folds and validation losses mostly concentrated in the order of 10^{-6}. The corresponding test set R^2 values ranged from 0.9701 to 0.9939, maintaining a generally high level, while test losses were also controlled within 10^{-6} to 10^{-5}, demonstrating that the training strategy retained effective error control under different loading modes. Overall, both models exhibited high stability and strong generalization capability across different data partitions through the same rigorous cross-validation procedure. They consistently showed reliable application potential in complex mechanical scenarios, thereby jointly verifying the effectiveness and engineering applicability of the adopted network architecture, training methodology, and regularization strategies in predicting the mechanical behavior of woven fabrics.

The Monte Carlo Dropout method was employed to quantify the uncertainty in model predictions. During implementation, the Dropout layers were kept active after model training, and 100 forward passes were performed on the test set to obtain the statistical properties of the predictive distribution. Based on these results, the mean and standard deviation were calculated, and the 95% confidence interval was determined, as illustrated in Fig. 18. The results show that the mean prediction curves for both axial and bias tensile responses exhibit excellent agreement with the actual test data points. The uncertainty bands encompass the majority of the experimental data across the entire stress–strain path, and the confidence band maintains a narrow width over a large strain range. These findings fully demonstrate that the model not only maintains high predictive accuracy but also possesses excellent reliability.

4.4. Generalization capability of neural network models

To verify the prediction accuracy of the trained neural network architecture, this study selected a twill fabric structure (5-5-1 configuration) as the research subject. Comparative analysis between finite element analysis results and neural network predictions (Figs. 19(a)

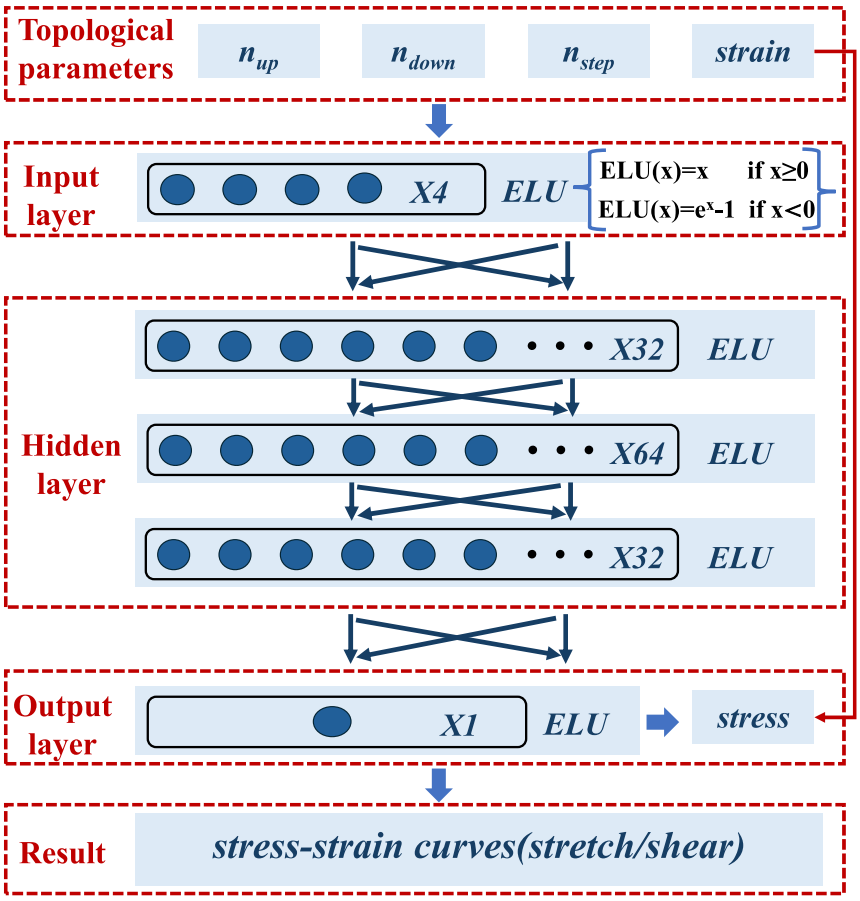

Fig. 15. Artificial neural network architecture.

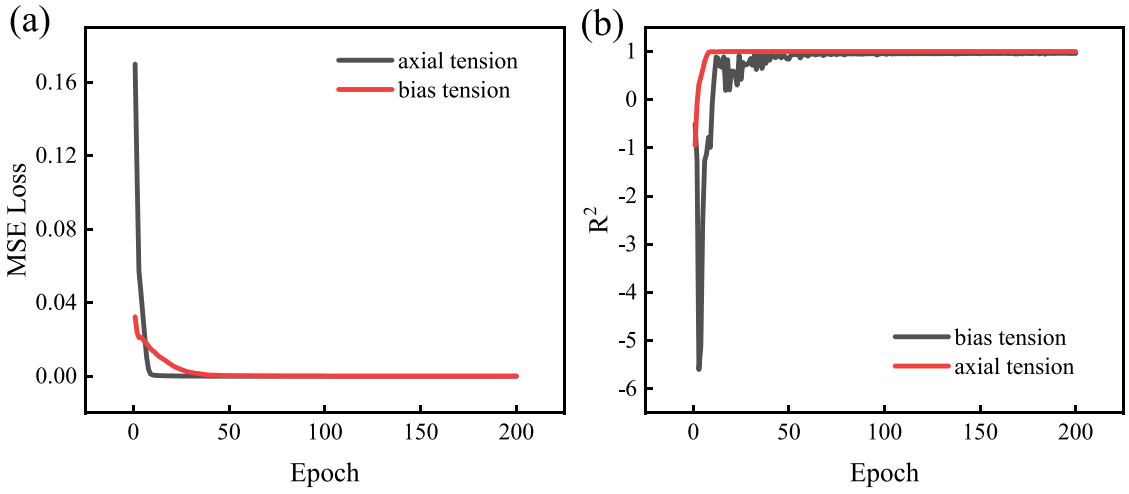

Fig. 16. (a) The variation of mean squared error loss during the neural network training process. (b) R^2 variation during the neural network training process.

and 19(b)) demonstrated excellent agreement in both bias and axial tensile curves, confirming the neural network's predictive accuracy. In terms of computational efficiency, obtaining the bias tensile curve for this fabric structure (5-5-1) using finite element methods required over 11 h on a 32-core CPU, while the axial tensile curve demanded more than 67 h. In contrast, the neural network prediction method could acquire the mechanical property curves of the fabric structure within 10 s, representing a three-order-of-magnitude improvement in computational efficiency (from hours to seconds). This remarkable efficiency advantage demonstrates that using neural networks for predicting fabric mechanical properties can significantly reduce time costs, providing an efficient technical approach for subsequent systematic

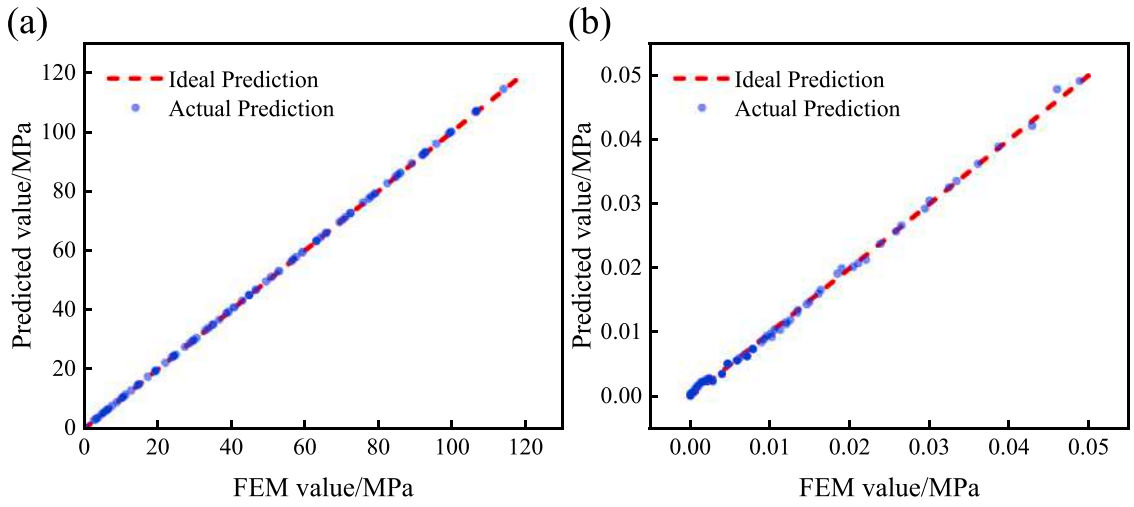

Fig. 17. (a) Neural network predictions vs. FEM benchmarks for axial tensile behavior. (b) Neural network predictions vs. FEM benchmarks for 45° bias tensile behavior.

Table 4
Model Performance Across Different Folds.

Fold	Type	best_val_R^2	best_val_Loss	cor_test_R^2	**cor_test_Loss**
1	Axial Tensile	0.999885125	9.30132×10^{-6}	0.999117915	8.88233×10^{-5}
2	Axial Tensile	0.999919223	5.46393×10^{-6}	0.999409977	5.94135×10^{-5}
3	Axial Tensile	0.999778057	1.6641×10^{-5}	0.99919613	8.09473×10^{-5}
4	Axial Tensile	0.999909736	7.92471×10^{-6}	0.999742023	2.59775×10^{-5}
5	Axial Tensile	0.999898878	8.45000×10^{-6}	0.999335519	6.69112×10^{-5}
1	Bias Tensile	0.995718264	1.38845×10^{-4}	0.970143812	1.40135×10^{-5}
2	Bias Tensile	0.999888084	2.57430×10^{-6}	0.981888507	8.50095×10^{-6}
3	Bias Tensile	0.999805034	4.32077×10^{-6}	0.974275016	1.20745×10^{-5}
4	Bias Tensile	0.999886229	2.47124×10^{-6}	0.990138821	4.62852×10^{-6}
5	Bias Tensile	0.999804506	2.20362×10^{-6}	0.993890098	2.86738×10^{-6}

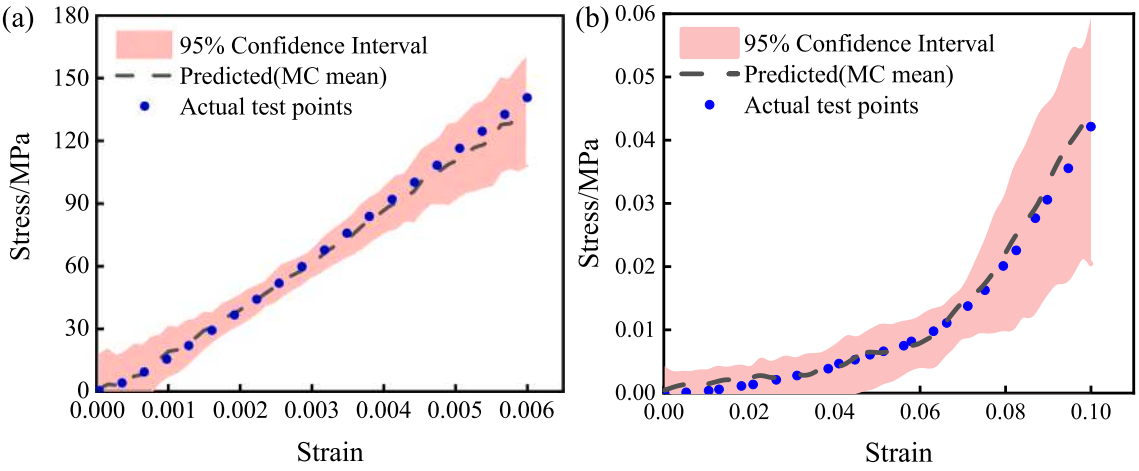

Fig. 18. (a) Comparison between the predicted mean and 95% confidence interval of stress–strain curve (axial tensile). (b) Comparison between the predicted mean and 95% confidence interval of stress–strain curve (bias tensile).

studies on the influence of fabric architectural topological parameters on mechanical properties.

5. Parametric analysis results of fabric mechanical properties

The influence of unit cell architectural topological parameters on the mechanical properties of fabrics was systematically analyzed through combined finite element method and artificial neural network predictions. The parameter n_{step} is constrained by n_{up} and n_{down}: when $n_{step} \geq 2$, the fabric adopts a satin structure, requiring the number of warp and weft yarns in the unit cell to satisfy $n_{up}+n_{down} \geq 5$ (excluding 6), with $1 < n_{step} < n_{up} + n_{down} - 1$ and no common divisors between n_{step} and $n_{up} + n_{down}$. As illustrated in Fig. 20, to evaluate the effects of n_{up} and n_{down}, the analysis was first conducted with $n_{step} = 1$ under two conditions:

- for unequal n_{up} and n_{down} : the correlation between the ratio $\max(n_{up}, n_{down})/\min(n_{up}, n_{down})$ and the mechanical properties was examined
- for equal n_{up} and n_{down} : the influence of absolute parameter values on mechanical behavior was assessed

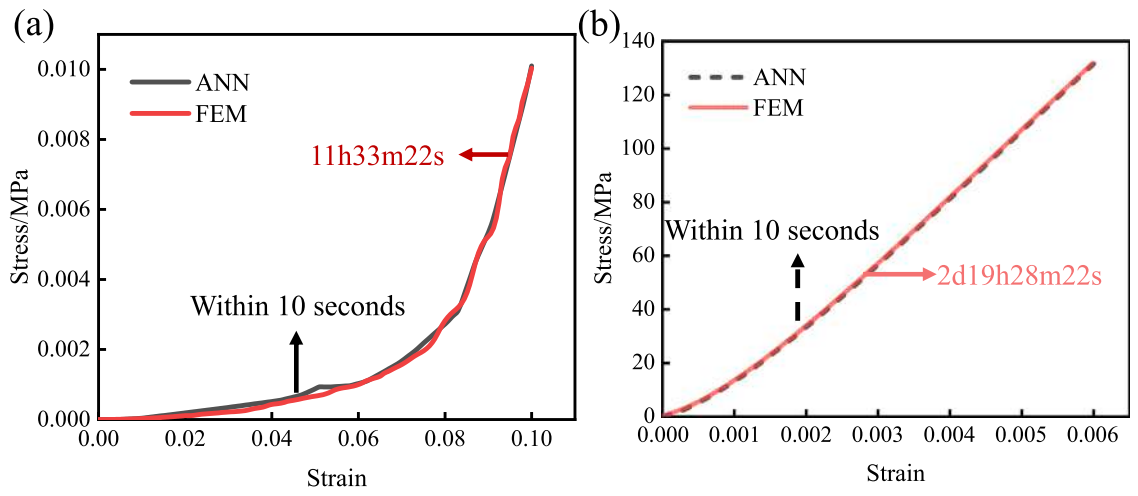

Fig. 19. (a) Bias tensile curve of twill fabric (5-5-1) obtained based on neural network methods and finite element analysis. (b) Axial tensile curve of twill fabric (5-5-1) obtained from neural network methods and finite element analysis.

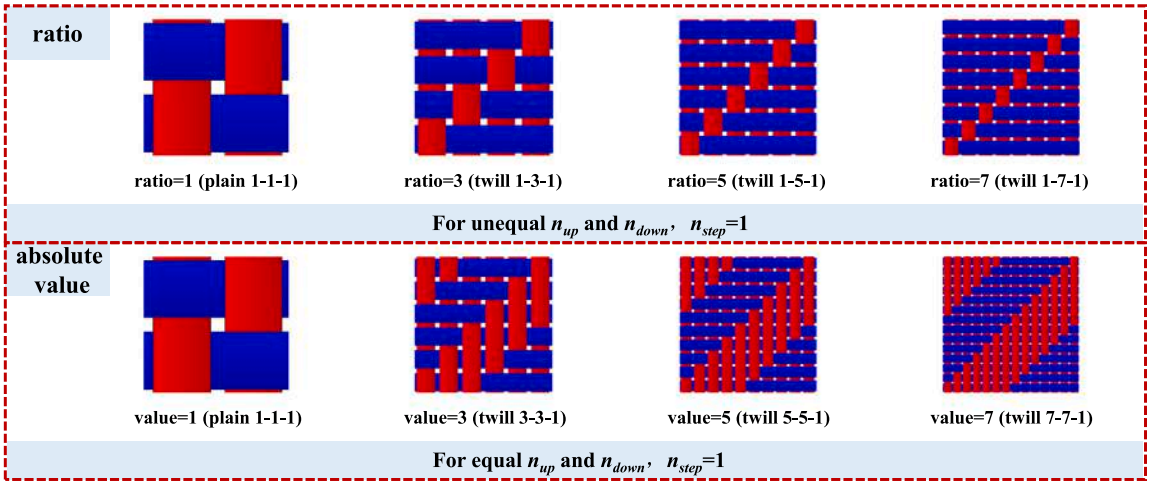

Fig. 20. Schematic illustrations of fabric unit cell structures with different topological parameters.

Following this initial analysis, specific values of n_{up} and n_{down} were selected, and n_{step} was systematically varied to investigate its impact on the fabric's mechanical performance.

5.1. Fabric shear performance

(1) The influence of architectural topological parameters ratio $\max(n_{up}, n_{down})/\min(n_{up}, n_{down})$ on the shear properties of woven fabrics

Finite element analysis and artificial neural network simulations were employed to investigate the bias tensile behavior of fabrics with varying architectural topological parameters ratios (Fig. 21(a)). The results revealed a consistent trend where stress under identical strain conditions decreased with increasing parameter ratio $\max(n_{up}, n_{down})/\min(n_{up}, n_{down})$, with the magnitude of stress reduction diminishing at higher ratios. The most significant stress reduction (68.9%, from 0.45 MPa to 0.14 MPa at 0.1 strain) occurred during the transition from plain weave (1-1-1) to twill weave (1-2-1), while minimal reduction (11.9%, from 0.042 MPa to 0.037 MPa) was observed when transitioning from 1-6-1 to 1-7-1 structures, where curves exhibited strong initial overlap. These mechanical behaviors can be rationally explained by textile mechanisms: The yarn interlacing points provide structural stability by resisting slippage, while the increased parameter ratio leads to longer float lengths and reduced interlacing density, significantly compromising the fabric's shear resistance and consequently resulting in observed stress reduction under identical strain conditions. This mechanism is substantiated by the shear stress distribution characteristics of twill weaves (1-2-1 and 2-2-1) (Fig. 21(e) and (f)): the stress values at interlacing regions are markedly higher than in non-interlacing zones, confirming the restraining effect of interlacing points on slippage; the 2-2-1 twill weave with longer float lengths exhibits significantly lower overall stress levels compared to the 1-2-1 structure, visually demonstrating the negative correlation between float length effects and mechanical performance. However, this effect becomes less pronounced at higher ratios as the marginal influence of float length extension diminishes, resulting in reduced variability between stress–strain curves.

(2) The influence of architectural topological parameters n_{skip} on the shear properties of woven fabrics

When the parameters n_{up} and n_{down} share identical values (denoted as n_{skip}), their ratio $\max(n_{up}, n_{down})/\min(n_{up}, n_{down})$ becomes unity.

In this scenario, the impact of n_{skip} magnitude on fabric mechanical properties was systematically analyzed through combined finite element analysis and artificial neural network approaches. Fig. 21(b) presents the resulting bias tensile curves, which exhibit trends consistent with Fig. 21(a): fabric stress at constant strain decreases monotonically with increasing n_{skip}, though the rate of decrease attenuates at higher n_{skip} values. The most substantial stress reduction (82.2%) occurs during the transition from plain weave (1-1-1) to twill

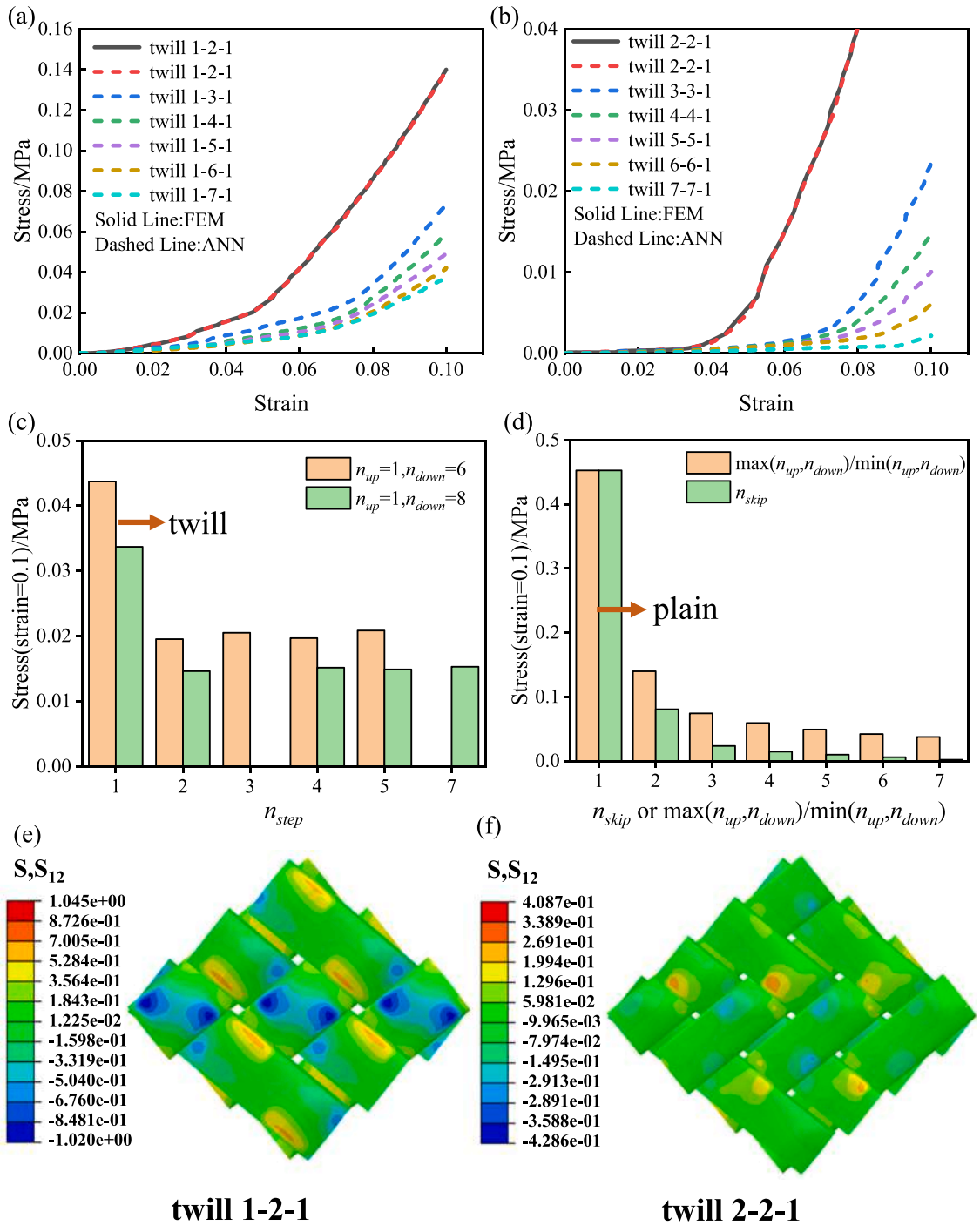

Fig. 21. (a) The stress — strain curve diagram of fabric off — axis tensile stress for different architectural topological parameters ratios of $\max(n_{up}, n_{down})/\min(n_{up}, n_{down})$. (b) The stress–strain curve diagram of fabric off — axis tensile stress for different architectural topological parameters n_{skip}. (c) The bias tensile stress values of fabrics with different parameter n_{step} (strain=0.1). (d) The bias tensile stress values of fabrics with different architectural topological parameters (strain=0.1). (e) Finite element analysis of the bias tensile performance of twill weave (1-2-1) fabric. (f) Finite element analysis of the bias tensile performance of twill weave (2-2-1) fabric.

weave (2-2-1), with stress at 0.1 strain dropping from 0.45 MPa to 0.08 MPa (Fig. 21(d)). Longitudinal comparison of shear resistance effects (evaluated at $\varepsilon = 0.1$), Fig. 21(d) reveals that both $\max(n_{up}, n_{down})/\min(n_{up}, n_{down})$ and n_{skip} produce similarly trending curves. Notably, except for the plain weave (1-1-1), the n_{skip} curve consistently lies below the ratio curve, indicating systematically weaker shear resistance. This phenomenon arises because equivalent numerical values (excluding unity) yield longer float lengths and consequently reduced structural reliability in n_{skip} parameterized fabrics.

(3) The influence of architectural topological parameters n_{step} on the shear properties of woven fabrics

The parameter n_{step} is functionally dependent on n_{up} and n_{down}, and its influence on fabric mechanics was systematically evaluated through two representative structural configurations: (i) $n_{up} = 1$, $n_{down} = 6$ with all permissible n_{step} values, and (ii) $n_{up} = 1$, $n_{down} = 8$ with all valid n_{step} variations (Fig. 22). As shown in Fig. 21(c), increasing n_{step} from 1 to 2 induces a critical structural transition from twill to satin weave, accompanied by significant stress reduction at constant strain

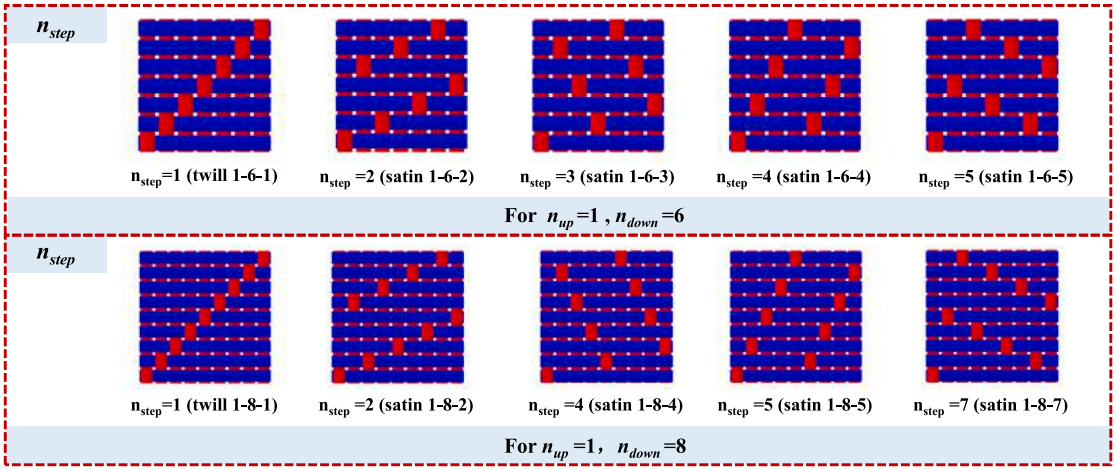

Fig. 22. Schematic illustrations of fabric unit cell structures with different n_{step}.

(strain=0.1) and marked decrease in shear resistance. However, for $n_{step} > 2$, the stress values exhibit stable fluctuations without further statistically significant reduction, as the fabric maintains satin weave topology while only generating geometrically distinct variants that preserve the fundamental yarn interaction mechanism governing shear resistance. This mechanical stabilization explains the observed equilibrium in shear properties across different satin structures at higher n_{step} values.

5.2. Fabric tensile performance

(1) The influence of architectural topological parameters ratio $\max(n_{up}, n_{down})/\min(n_{up}, n_{down})$ on the tensile properties of woven fabrics

The axial tensile curves of fabrics with varying architectural topological parameters ratios were obtained through finite element analysis and artificial neural networks, as illustrated in Fig. 23(a). All fabrics exhibited a consistent stress trend: under identical strain conditions, the stress increased with the parameter ratio $\max(n_{\text{up}}, n_{\text{down}})/\min(n_{\text{up}}, n_{\text{down}})$. Comparative analysis with Fig. 23(b) revealed that the axial tensile modulus and stress value (at strain = 0.006) exhibited diminishing returns with increasing ratio. The most significant enhancement occurred when the ratio increased from 1 to 2, corresponding to a transition from plain weave (1-1-1) to twill weave (1-2-1). Specifically, the tensile modulus rose from 11.9 GPa to 16.1 GPa (a 35.3% increase), while the stress at strain = 0.006 increased from 64.7 MPa to 82.5 MPa (a 27.5% increase). In contrast, the transition from 1-6-1 to 1-7-1 resulted in only a 3% increase in tensile modulus and a 3.8% increase in stress.

These observations can be interpreted through principles of textile science. Fabrics with more interlacing points and shorter float lengths exhibit greater yarn bending, leading to reduced resistance to tensile deformation. As the parameter ratio $\max(n_{\text{up}}, n_{\text{down}})/\min(n_{\text{up}}, n_{\text{down}})$ increases, the float length extends, the number of interlacing points per unit area declines, and yarn bending diminishes. Consequently, the axial tensile modulus and stress under fixed strain conditions rise with the parameter ratio. However, the marginal effect of further increasing the float length becomes less pronounced, resulting in smaller variations and higher coincidence in the stress–strain curves.

(2) The influence of architectural topological parameters n_{skip} on the tensile properties of woven fabrics

The axial tensile curves for fabrics with varying n_{skip} values are presented in Fig. 23(c). The trend parallels that of Fig. 23(a): both the axial tensile modulus and stress at constant strain increase with n_{skip}, albeit at a decreasing rate. The most substantial improvement occurred during the transition from plain weave (1-1-1) to twill weave (2-2-1), where the tensile modulus surged by 63% (from 11.9 GPa to 19.4 GPa) and the stress at strain = 0.006 increased by 48.2% (from 64.7 MPa to 95.9 MPa).

(3) The influence of architectural topological parameters n_{step} on the tensile properties of woven fabrics

Consistent with the previous analysis of fabric shear resistance, the influence of parameter n_{step} on axial tensile properties was systematically investigated through examination of two distinct fabric configurations: (i) $n_{up} = 1$, $n_{down} = 6$ with all permissible n_{step} values, and (ii) $n_{up} = 1$, $n_{down} = 8$ with all valid n_{step} variations. Comparative analysis of the results (Fig. 23(e)–(f)) reveals that neither the axial tensile modulus nor the tensile stress at strain = 0.006 exhibits dependence on n_{step}. Instead, these mechanical properties are solely determined by the architectural topological parameters n_{up} and n_{down}. This observation can be explained by fundamental fabric mechanics: The axial tensile behavior of woven fabrics is primarily governed by yarn bending deformation along the loading direction, rather than being influenced by the geometric arrangement of yarns as characterized by n_{step}.

5.3. Correlation analysis between mechanical properties and architectural topological parameters of 2D woven fabrics

Using the architectural topological parameters of the fabric unit cell (n_{up}, n_{down}, n_{step}) as input variables and the modulus of the axial tensile stress–strain curve (denoted as n_{modulus}) and the stress value at a strain of 0.1 for the bias tensile stress–strain curve (denoted as n_{stress}) as representative output parameters, a unified dataset was constructed.

The Pearson linear correlation coefficient (Eq. (11)) was employed to quantify the relationships between the variables, and a heatmap (Fig. 24) was generated using the Seaborn library. The results indicate that the output parameter modulus(axial) exhibits strong positive correlations with the input variables n_{up} and n_{down} ($r = 0.47$ and $r = 0.78$, respectively), with the correlation to ndown being particularly significant. In contrast, the correlation coefficient between modulus(axial) and n_{step} is only 0.13, indicating a weak relationship. For stress(bias), the correlation coefficients with n_{up} and n_{down} are −0.55 and −0.41, respectively, demonstrating moderate negative correlations, which suggests that stress(bias) decreases as n_{up} or n_{down} increases. Meanwhile, the correlation coefficient between stress(bias) and n_{step} is −0.02, indicating almost no linear relationship. A particularly important finding is the strong negative correlation (r = −0.84) between the two output parameters, modulus(axial) and stress(bias), which implies that the

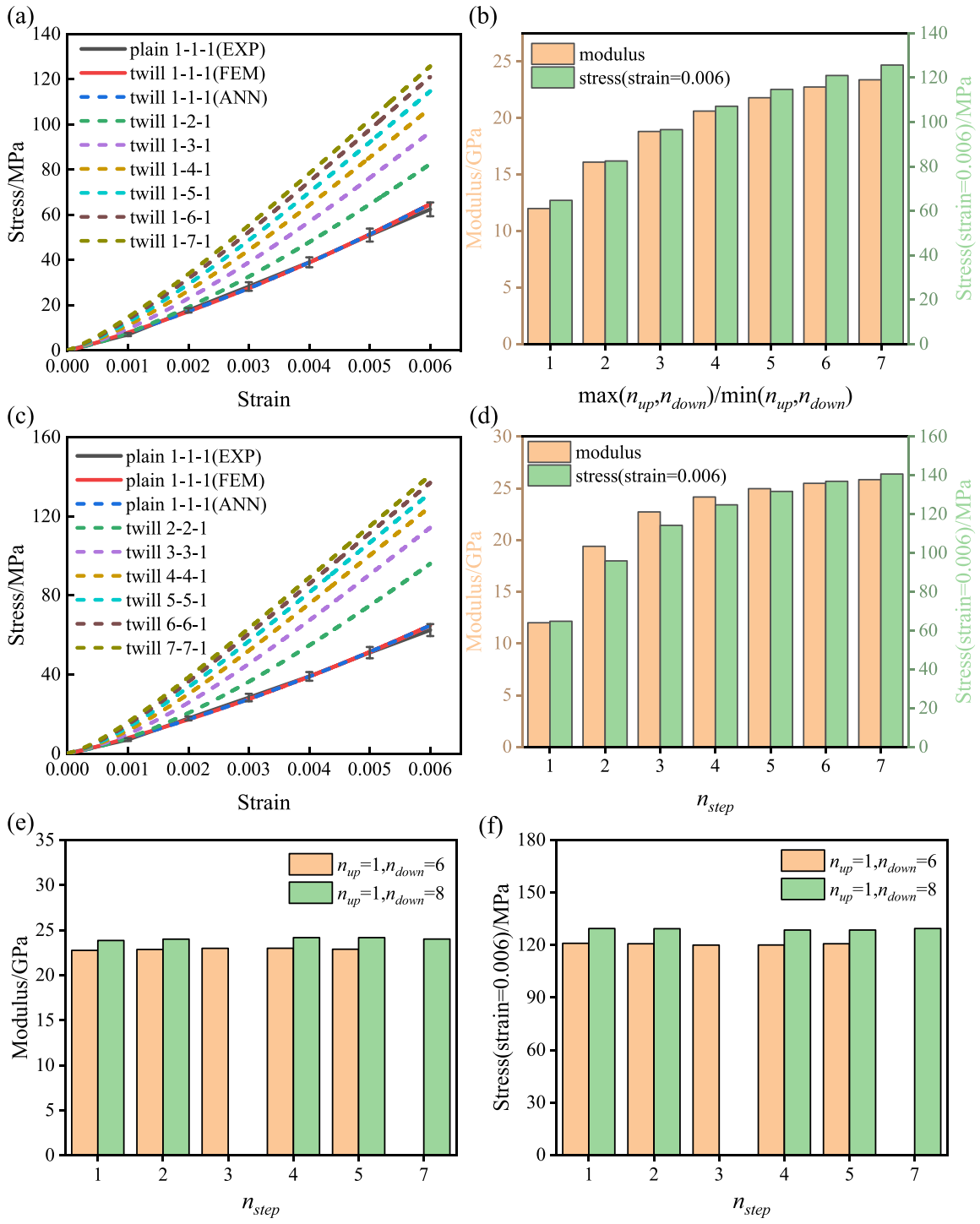

Fig. 23. (a) The stress–strain curve diagram of fabric axial tensile stress for different architectural topological parameters ratios of $\max(n_{up}, n_{down})/\min(n_{up}, n_{down})$. (b) The axial tensile modulus and stress distribution (strain = 0.006) of fabrics with different architectural topological parameters ratios $\max(n_{up}, n_{down})/\min(n_{up}, n_{down})$. (c) The stress–strain curve diagram of fabric axial tensile stress for different architectural topological parameters n_{skip}. (d) The axial tensile modulus and stress distribution (strain = 0.006) of fabrics with different architectural topological parameters n_{skip}. (e) Distribution of axial tensile modulus of fabrics with different parameter n_{step}. (f) Distribution of axial stress of fabrics with different parameter n_{step} (strain = 0.006).

fabric structure cannot simultaneously achieve excellent axial tensile resistance and shear resistance.

$$r = \frac{\mathrm{cov}(X, Y)}{S_X S_Y} \tag{11}$$

Where X represents the input variable, Y denotes the output variable, cov stands for covariance, and S indicates the standard deviation.

6. The fabric integrated resistance factor

As demonstrated in the preceding analysis, the mechanical properties of fabric structures exhibit an inverse relationship with respect to architectural topological parameters: increasing the parameter ratio or value leads to a systematic decrease in shear resistance while simultaneously enhancing tensile strength. This trade-off presents a significant

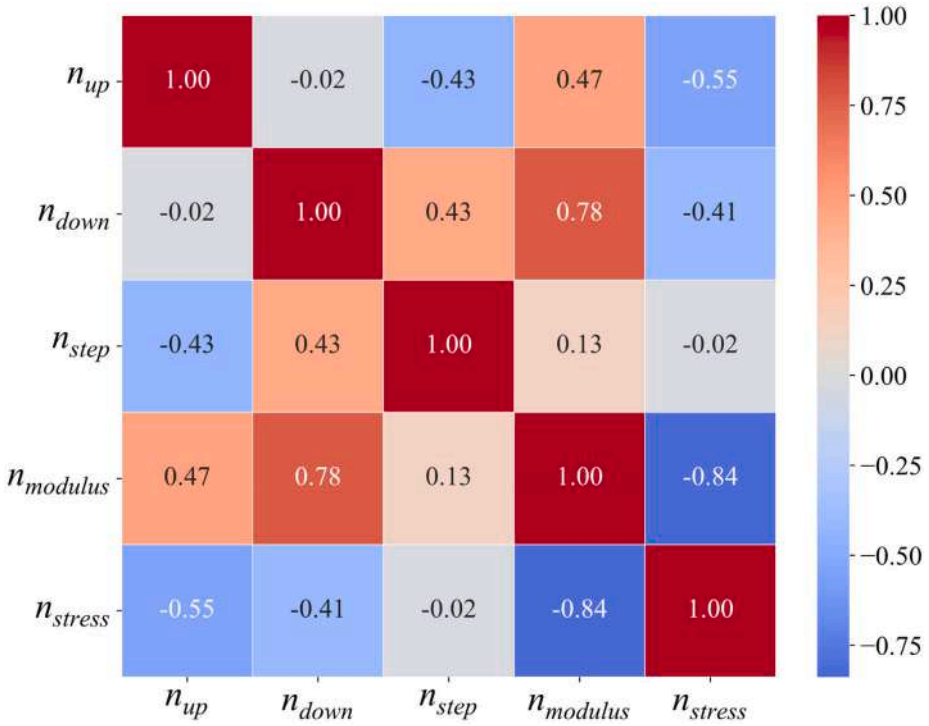

Fig. 24. Heatmap of correlation between mechanical properties and architectural topological parameters of 2D woven fabrics.

challenge when designing flexible thermal protection systems using ceramic fiber fabrics, where optimal performance requires both high shear resistance and superior tensile strength. Given the non-intuitive nature of fabric structure selection based on these competing mechanical properties, a novel fabric integrated resistance factor is introduced to enable comprehensive evaluation of both shear and tensile resistance characteristics. The mathematical formulation of this factor is presented in Eq. (12):

$$k = w \cdot \left(\frac{E}{E_{\max}}\right) + (1-w) \cdot \left(\frac{\sigma_{strain}}{\sigma_{\max}}\right) \tag{12}$$

In the equation, where σ_{strain} represents the stress value of the fabric at a certain strain during bias extension, $\sigma_{\max}$ represents the maximum stress value at the corresponding strain during bias extension for all fabrics with a architectural topological parameters within 7, E represents the modulus value of the fabric in the axial direction, and $E_{\max}$ represents the maximum modulus value in the axial direction for all fabrics with a architectural topological parameters within 7. w represents the weight of the axial tensile deformation in the fabric plane deformation.

(1) The Influence of Strain on the Integrated Resistance Factor of Fabric Structures

In cases where the mechanical behavior of fabric structures under both axial tension and shear must be considered concurrently, a weight coefficient $w = 0.5$ is assigned. Based on the established neural network model, five strain levels ($\varepsilon = 0.06, 0.07, 0.08, 0.09, 0.1$) are selected within the strain range $[0.06, 0.1]$ at intervals of 0.01. The corresponding integrated resistance factors are calculated for each strain level, while the weight coefficient $w = 0.5$ is held constant throughout the analysis, enabling a systematic evaluation of the influence of strain variation on the assessment results.

The analysis indicates that the integrated resistance factor k demonstrates good robustness within the investigated strain range. As shown in Figs. 25(a) and 25(b), with the weight coefficient fixed at $w = 0.5$, the curves of the factor exhibit consistent trends across different strain levels: as the parameter ratio or its magnitude increases, the value of k initially decreases sharply and then stabilizes or experiences a slight rebound. This suggests that the indicator can reliably capture the influence of fabric structural changes on mechanical performance. Notably, the plain weave fabric (1-1-1) consistently maintains the highest integrated resistance factor across all strain conditions. This demonstrates that the plain weave consistently outperforms other configurations in balancing axial and shear behavior. Its superiority is thus independent of the strain target selected. Furthermore, as the strain value increases from 0.06 to 0.1, the shape and relative positions of the curves show no significant shift, with only systematic minor adjustments in magnitude. This implies that variations in strain do not lead to a reversal in the ranking order among different structural configurations.

In summary, the integrated resistance factor k exhibits low sensitivity to the chosen strain target and maintains stable evaluation capability within a reasonable strain range. These characteristics confirm its suitability for application in multi-objective optimization of woven fabrics.

(2) The Influence of w on the Integrated Resistance Factor of Fabric Structures

When the application scenario emphasizes either axial tension or shear deformation in the fabric's mechanical behavior, the weight coefficient is adjusted accordingly. To quantitatively analyze the influence of weight assignment, this study systematically compares weight coefficients w ranging from 0.3 to 0.7 in increments of 0.1, with the strain value fixed at $\varepsilon = 0.1$.

As shown in Figs. 26(a) and 26(b), the variation of the integrated resistance factor with fabric structural parameters exhibits highly consistent trends under different weight values: when the fabric structure transitions from plain weave to twill weave, the integrated resistance factor decreases significantly; as the structural parameter ratios or values continue to increase, the factor gradually recovers and eventually stabilizes. This indicates that the factor can consistently reflect the trade-off in mechanical performance during fabric topological evolution, and its variation pattern remains insensitive to the choice of weight. Notably, the plain weave fabric (1-1-1) demonstrates stable performance across different weight settings: within the weight range of $w \leq 0.6$, the plain weave consistently maintains the highest integrated resistance factor, highlighting its significant advantage in

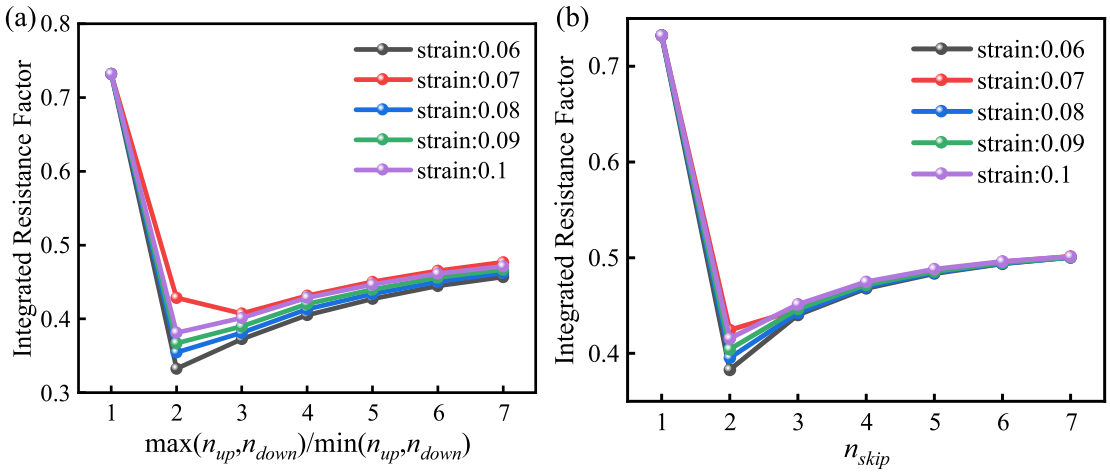

Fig. 25. (a) Variation of the integrated resistance factor with the architectural topological parameters ratio under different strain conditions (w = 0.5). (b) Variation of the integrated resistance factor with the numerical values of architectural topological parameters under different strain conditions (w = 0.5).

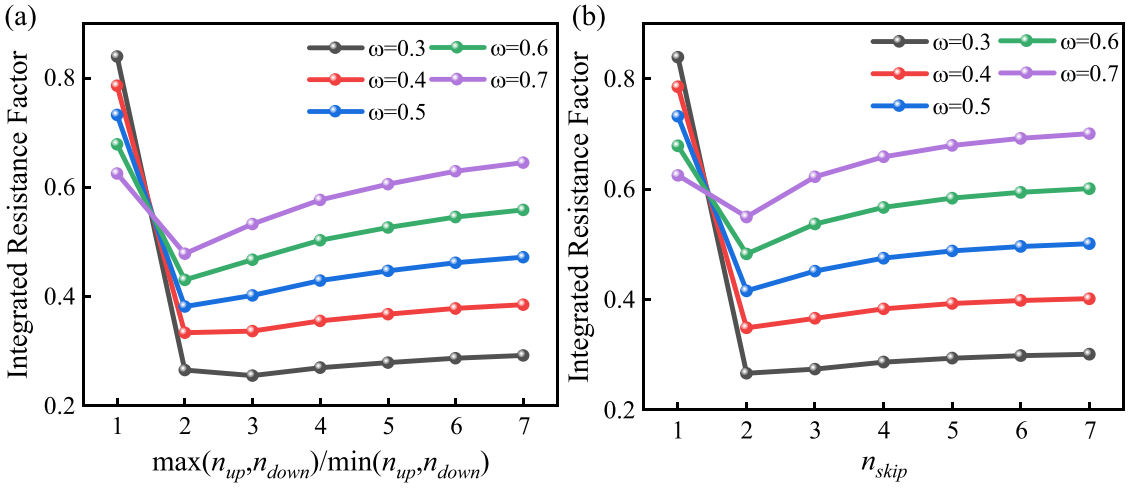

Fig. 26. (a) Variation of the integrated resistance factor with the architectural topological parameters ratio under different weights (ε = 0.1). (b) Variation of the integrated resistance factor with the numerical values of architectural topological parameters under different weights (ε = 0.1).

balancing tensile and shear properties. Even under the condition of w = 0.7 (where greater emphasis is placed on tensile stiffness), the integrated resistance factor of the plain weave, although not reaching the maximum value, remains close to the optimum with only a 10.8% difference, indicating its overall competitive performance. These results suggest that within a reasonable range of engineering preferences ($w \in [0.3, 0.6]$), the plain weave is consistently the optimal choice. Moreover, even in design scenarios that favor tensile performance (w = 0.7), its performance remains highly competitive.

Notably, this analysis excludes the influence of parameter n_{step} on the integrated resistance factor. This exclusion is justified by the parameter's unique effect on fabric properties: while increasing n_{step} degrades shear resistance, it maintains constant tensile resistance. Consequently, for fabrics with identical n_{step} and n_{down} parameters, a satin weave fabric ($n_{\text{step}} > 1$) will invariably exhibit a lower integrated resistance factor compared to its twill weave counterpart with $n_{\text{step}} = 1$.

7. Conclusion

This study presents a comprehensive methodology for analyzing fabric architectural topological parameters' influence on mechanical performance, with applications to deformable skin design for high-mach-number flight vehicles. An integrated computational framework combining parametric modeling and finite element analysis was developed to characterize periodic rhombic preforms' mechanical behavior under single-cell boundary conditions. The research establishes three key advances: First, fabric parameterization was simplified through characterization of common 2D woven structures (plain, satin, and twill weaves) using three fundamental parameters (n_{up}, n_{down}, and n_{step}). Second, a high-throughput computational platform was developed to generate an extensive mechanical property database, enabling creation of an artificial neural network model that accurately predicts tensile and shear properties for fabrics with architectural topological parameters (achieving >98% prediction accuracy in <10 s per simulation). Third, systematic analysis revealed distinct parameter-property relationships: increasing n_{up}/n_{down} ratios enhances tensile resistance (up to 63%) while reducing shear resistance (up to 82.8%), whereas n_{step} exclusively affects shear properties without influencing tensile behavior. The proposed integrated resistance factor (the plain weave fabric exhibits the optimal performance) effectively evaluates the tensile/shear resistance balance, providing critical design guidelines for aerospace fabrics requiring simultaneous high tensile and shear performance.

CRediT authorship contribution statement

Zhou Jiang: Writing – original draft, Visualization. **Mingming Xu:** Writing – review & editing, Methodology. **Jian Sun:** Project administration, Funding acquisition. **Jinsong Leng:** Supervision, Funding acquisition.

Data and code availability statement

The data and code supporting this study are available in a GitHub repository at https://github.com/mintg911/WovenFabricPredictor-ANN. This repository contains a neural network-based surrogate modeling framework for rapid prediction of 2D woven ceramic fabric mechanical properties. It includes the full source code, pretrained models, training and validation datasets, and additional utilities to support reuse and validation.

Declaration of competing interest

The authors declare that they have no known competing financial interests or personal relationships that could have appeared to influence the work reported in this paper.

Data availability

Data will be made available on request.

References

[1] Sun J, Guan Q, Liu Y, Leng J. Morphing aircraft based on smart materials and structures: A state-of-the-art review. J Intell Mater Syst Struct 2016;27(17):2289–312.

[2] Sun J, Liu Y, Leng J. Mechanical properties of shape memory polymer composites enhanced by elastic fibers and their application in variable stiffness morphing skins. J Intell Mater Syst Struct 2015;26(15):2020–7.

[3] Smith CR. Aerodynamic heating in hypersonic flows. Phys Today 2021;74(11):66–7.

[4] Mui D, Clancy H. Development of a protective ceramic coating for shuttle orbiter advanced flexible reusable surface insulation (AFRSI). In: Proceedings of the 9th annual conference on composites and advanced ceramic materials: ceramic engineering and science proceedings, vol. 6, Wiley Online Library; 1985, p. 793–805.

[5] Sawko PM, Goldstein HE. Tailorable advanced blanket insulation (TABI). NASA Tech Briefs 1987;11(ARC-11697).

[6] Behrens B. Technologies for thermal protection systems applied on re-usable launcher. In: 54th international astronautical congress of the international astronautical federation, the international academy of astronautics, and the international institute of space law. 2004, p. IAA–13.

[7] Rezin M, Oka K, Arnold J. The evolution of flexible insulation as thermal protection systems for reusable launch vehicles: AFRSI (advanced flexible reusable surface insulation) to CRI (conformal reusable insulation). In: National space and missile materials symposium. 2001.

[8] Wercinski P. Adaptable deployable entry & placement technology (ADEPT) for cubesat delivery to mars surface. In: Mars cubeSat/nanoSat workshop. (ARC-E-DAA-TN19332). 2014.

[9] DiNonno J, Cheatwood N. Low-earth orbit flight test of an inflatable decelerator (loftid) mission overview and science return. In: AIAA SCITECH 2024 forum. 2024, p. 1309.

[10] Smith B, Venkatapathy E, Wercinski P, Yount B, Prabhu D, Gage P, Glaze L, Baker C. Venus in situ explorer mission design using a mechanically deployed aerodynamic decelerator. In: 2013 IEEE aerospace conference. IEEE; 2013, p. 1–18.

[11] Chen G, Guo K, Chen C, Chang M, Wang R, Tang E. Thermal-dynamic response of flexible composite structures under combined thermal flux and tensile loading. Int J Therm Sci 2025;210:109607.

[12] Owens W, Merkel D, Sansoz F, Fletcher D. Fracture behavior of woven silicon carbide fibers exposed to high-temperature nitrogen and oxygen plasmas. J Am Ceram Soc 2015;98(12):4003–9.

[13] Mazaheri A, Bruce, III WE, Mesick NJ, Sutton K. Methodology for flight-relevant arc-jet testing of flexible thermal protection systems. J Spacecr Rockets 2014;51(3):789–800.

[14] Azeem M, Ahmad Z, Wiener J, Fraz A, Siddique HF, Havalka A. Influence of weave design and yarn types on mechanical and surface properties of woven fabric. Fibres Text East Eur 2018;26(1 (127)).

[15] Zhang W, He J, Li J, Li Q, He C, Li W. Influence of fabric structures and temperature on the mechanical properties of quartz braids. Text Res J 2024;94(9–10):1002–11.

[16] Liu G, Yu P, Tao Y, Liu T, Liu H, Zhao J. Hybrid 3D printed three-axis force sensor aided by machine learning decoupling. Int J Smart Nano Mater 2024;15(2):261–78.

[17] Lin X, Li Y, Lei Y, Sun Q. Electric-double-layer-gated 2D transistors for bioinspired sensors and neuromorphic devices. Int J Smart Nano Mater 2024;15(1):238–59.

[18] Wu C, Xiao Z, Guo Y, Zhang C. Analysis of nonlinear multi-field coupling responses of piezoelectric semiconductor rods via machine learning. Int J Smart Nano Mater 2024;15(1):62–74.

[19] Li X, Ning S, Liu Z, Yan Z, Luo C, Zhuang Z. Designing phononic crystal with anticipated band gap through a deep learning based data-driven method. Comput Methods Appl Mech Engrg 2020;361:112737.

[20] Li X, Liu Z, Cui S, Luo C, Li C, Zhuang Z. Predicting the effective mechanical property of heterogeneous materials by image based modeling and deep learning. Comput Methods Appl Mech Engrg 2019;347:735–53.

[21] Yin B, Huang J, Sun W. Peridynamics-fueled convolutional neural network for predicting mechanical constitutive behaviors of fiber reinforced composites. Comput Methods Appl Mech Engrg 2024;431:117309.

[22] Ahirwar M, Behera B. Prediction of tear strength of bed sheet fabric using machine learning based artificial neural network. J Text Inst 2024;115(1):22–8.

[23] Rolich T, Šajatović AH, Pavlinić DZ. Application of artificial neural network (ANN) for prediction of fabrics' extensibility. Fibers Polym 2010;11:917–23.

[24] Wanasinghe C, Dharmawansha S, Ariyasinghe N, Ranatunga P, Herath S, Mallikarachchi C, Meddage D. Multiscale modelling and explainable AI for predicting mechanical properties of carbon fibre woven composites with parametric microscale and mesoscale configurations. Compos Struct 2025;369:119282.

[25] Gurumurthy B. Prediction of fabric compressive properties using artificial neural networks. AUTEX Res J 2007;7(1):19–31.

[26] Xu M, Sitnikova E, Li S. Unification and parameterisation of 2D and 3D weaves and the formulation of a unit cell for composites made of such preforms. Compos Part A: Appl Sci Manuf 2020;133:105868.

[27] Lin H, Brown LP, Long AC. Modelling and simulating textile structures using TexGen. Adv Mater Res 2011;331:44–7.

[28] Duan Y, Keefe M, Bogetti T, Cheeseman B. Modeling friction effects on the ballistic impact behavior of a single-ply high-strength fabric. Int J Impact Eng 2005;31(8):996–1012.

[29] Lee W, Padvoiskis J, Cao J, de Luycker E, Boisse P, Morestin F, Chen J, Sherwood J. Bias-extension of woven composite fabrics. Int J Mater Form 2008;1:895–8.